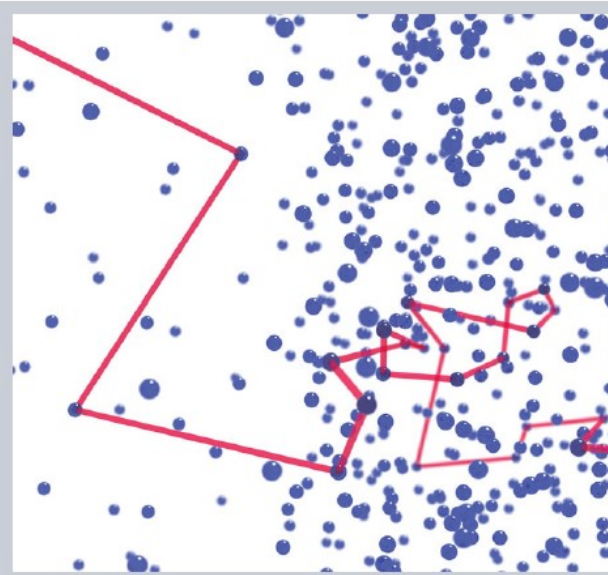


**Abstract** A major aim of researchers working in the field of optics and photonics is to mold the flow of light in optical structures and devices. In the regime of ballistic light propagation, transformation optics has given a certain boost, for which optical invisibility cloaking devices are striking examples. Our capability to mold the flow of light in the regime of diffuse light propagation in light-scattering media has fallen behind—while diffuse light from clouds, white wallpaper, computer monitors, and light-emitting diodes is literally all around us every day. In this review, we summarize progress in steering the flow of diffuse light in turbid media which was triggered by the mathematical analogy between electrostatics, magnetostatics, stationary heat conduction, and stationary light diffusion. We give an extensive tutorial introduction to the mathematics of the diffusion equation for light and its solutions, present an overview on the current experimental state-of-the-art of simple core–shell invisibility cloaking, and compare these experiments with diffusion theory as well as with more advanced modelling based on Monte Carlo simulations. The latter approach enables spanning the bridge from diffusive to ballistic light propagation.



## Invisibility cloaking in light-scattering media

Robert Schittny<sup>1</sup>, Andreas Niemeyer<sup>1</sup>, Frederik Mayer<sup>1</sup>, Andreas Naber<sup>1</sup>, Muamer Kadic<sup>1</sup>, and Martin Wegener<sup>1,2,\*</sup>

### 1. Introduction

You wake up, look out of your window and see blue sky originating from wavelength-dependent Rayleigh scattering of sunlight off of deep-sub-wavelength particles. You may also see some white clouds that get their wavelength-independent appearance from scattering of light off of larger water droplets. You continue seeing light emerging from disordered light-scattering media when looking at a glass filled with milk on your breakfast table or at an egg shell, at the white wallpaper in the room, or at your own hands. Scattered light is literally all around us. Yet, somehow, we are much less used to thinking about engineering the flow of light in disordered media than we are for transparent ordered media. Most textbooks of optics are filled with examples for solutions of the Maxwell equations for (ordered) continua but they tell little or nothing at all about disordered optical media.

Tailoring disorder in optics does have important technical applications though. For example, randomly distributed nanoparticles on the surface of thin-film solar cells have extensively been considered for enhancing the effective absorption and thereby increasing the solar cell energy-conversion efficiency [1–3]. Lighting via incandescent lamps or via more modern semiconductor light-

emitting diodes often exploits rough surfaces or randomly distributed nanoparticles to homogenize or out-couple light emission [4–8].

In ordinary optics, we mold the flow of light in lens systems, prisms, dielectric stacks, photonic crystals, waveguide, etc. by designing tailored spatial distributions of the refractive index of light  $n(\vec{r})$  [9]. We have centuries of experience in doing that. More recently, the design tool of transformation optics [10–18] has even enabled us to equivalently map fictitious yet intuitive (coordinate) transformations onto actual spatially inhomogeneous and generally anisotropic distributions of the refractive-index tensor  $\hat{\vec{n}}$ . In this fashion, invisibility cloaking, which was long thought to be mere phantasy or science fiction, has become a sound scientific possibility [19–27].

By analogy, molding the flow of light in disordered media can be accomplished by designing spatial distributions of scattering objects. For example, we can spatially tailor the local density of scattering particles. We will see below that light propagation in disordered media can often (but not always) be well described by a diffusion equation for the photon density [28–33]. In this case, we can design spatial distributions of the scalar diffusivity for light,  $D(\vec{r})$ , or tensor versions thereof,  $\hat{D}(\vec{r})$ , to achieve certain functionalities. Due to the enormously large vacuum speed

<sup>1</sup> Institute of Applied Physics, Karlsruhe Institute of Technology (KIT), 76128 Karlsruhe, Germany

<sup>2</sup> Institute of Nanotechnology, Karlsruhe Institute of Technology (KIT), 76021 Karlsruhe, Germany

\*Corresponding author: e-mail: martin.wegener@kit.edu

of light, the stationary version of the diffusion equation often suffices. In this case, the mathematical form of the stationary diffusion equation  $\vec{\nabla} \cdot (D \vec{\nabla} n_{\text{phot}}) = 0$  with diffusivity of light  $D$  is strictly identical to that of electrostatics for continua, namely  $\vec{\nabla} \cdot (\epsilon \vec{\nabla} \phi) = 0$  with electric permittivity  $\epsilon$  (also see Sect. 2.2). A quasi-static approximation is often used for mathematical modeling of nano-optics. Hence, we can directly take know-how from nano-optics and carry it over to diffusive optics. Some caution has to be exerted though regarding the boundary conditions of a scattering medium to air or vacuum.

In Sect. 2 of this review, we give an extensive overview of the theory of light diffusion and its applications. We start with a tutorial-style introduction into describing light propagation in turbid media with a diffusion equation (Sect. 2.1). More details on light-diffusion theory can, e.g., be found in Ref. [32]. We then show how anisotropic light diffusion can be achieved using laminates (Sect. 2.2) and utilized for the diffusive counterparts of transformation optics and invisibility cloaking (Sect. 2.3). As examples, we discuss diffusive free-space core–shell cloaking (Sect. 2.4) and the cloaking of contact wires on organic light-emitting diodes (Sect. 2.5). In Sect. 3, we summarize previously published experiments on core–shell cloaking in both the stationary (Sect. 3.1) and the transient (Sect. 3.2) regimes of diffusive light transport. Finally, before concluding, we explore in Sect. 4 the validity of the diffusion description for these applications by comparison with more advanced Monte Carlo simulations that can especially cope with the transition regime from diffuse to ballistic optics.

## 2. Diffusion theory

### 2.1. Brief tutorial

Light rays in a homogeneous medium propagate as straight lines. If randomly distributed identical scattering centers are added, each light ray performs a random walk as illustrated in Fig. 1. This random walk can be characterized by a scattering mean free path length  $l_{\text{scat}}$ . For a scattering cross section  $\sigma_{\text{scat}}$  and a number density of scattering centers  $n_{\text{scat}}$ , we have

$$l_{\text{scat}} = \frac{1}{\sigma_{\text{scat}} n_{\text{scat}}}. \quad (1)$$

In general, the scattering cross section depends on the wavelength of light  $\lambda$ . For the example of Rayleigh scattering, i.e., for off-resonant deep-sub-wavelength scattering centers, it scales according to  $\sigma_{\text{scat}} \propto 1/\lambda^4$ . Near resonances and for arbitrary particle sizes, the cross section can be obtained from Mie-scattering theory [34, 35]. We note that due to causality, even for a dielectric particle, a finite scattering cross section over an extended wavelength range is unavoidably connected to a finite (although possibly small) absorption cross section  $\sigma_{\text{abs}}$  via the Kramers–Kronig relations for the refractive index of the scattering object. Scattering and absorption cross sections of individual particles

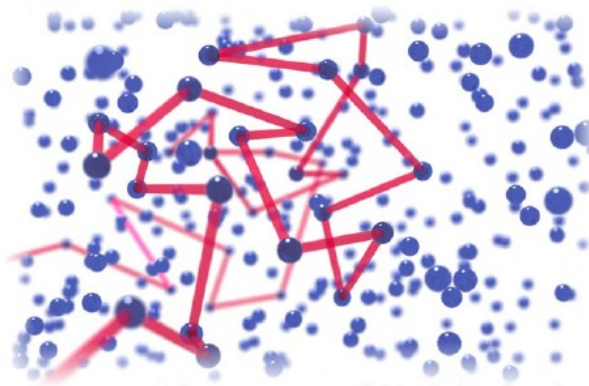


**Figure 1** Artistic illustration of light performing a random walk through a medium with randomly distributed scattering centers (blue spheres). Under the right conditions, light propagation through such a medium can be described by a diffusion equation for the photon density.

can be measured quantitatively [36, 37]. Additional absorption can originate from the molecules of the background medium the particles are embedded in, characterized by an absorption cross section of  $\sigma_{\text{abs}, \text{bg}}$  and a number density of  $n_{\text{bg}}$ . Which of the two effects dominates depends on the specific medium. Together, they lead to the absorption mean free path length

$$l_{\text{abs}} = \frac{1}{\sigma_{\text{abs}} n_{\text{scat}} + \sigma_{\text{abs}, \text{bg}} n_{\text{bg}}}. \quad (2)$$

The inverse of the scattering mean free path and the inverse of the absorption mean free path length are often referred to as scattering and absorption coefficients  $\mu_{\text{scat}}$  and  $\mu_{\text{abs}}$ , respectively.

According to Beer's law and assuming negligible absorption ( $l_{\text{abs}} \gg l_{\text{scat}}$ ), the intensity  $I(L)$  of light that has not scattered at all after propagation over a distance  $L$  along any one direction is given by

$$T_{\text{ball}} = \frac{I(L)}{I(0)} = \exp\left(-\frac{L}{l_{\text{scat}}}\right). \quad (3)$$

We shall refer to this ratio as the ballistic transmittance  $T_{\text{ball}}$ . Experimentally, one can send a monochromatic collimated laser beam with sufficiently small beam waist onto a homogeneous scattering medium with known thickness  $L$ . Behind the sample, an aperture in front of a detector collects only the solid angle of the transmitted laser beam and thereby suppresses scattered light, giving direct access to  $I(L)$ . By comparison with the undisturbed laser intensity  $I(0)$  (and verifying that the particles do not agglomerate), one can determine the scattering mean free path length for any given concentration of scattering particles from Eq. (3). A corresponding measurement on samples containing titania nanoparticles in a transparent polydimethylsiloxane (PDMS) matrix is shown in Fig. 2. PDMS is an optically transparent rubber-like silicone that can conveniently be processed.

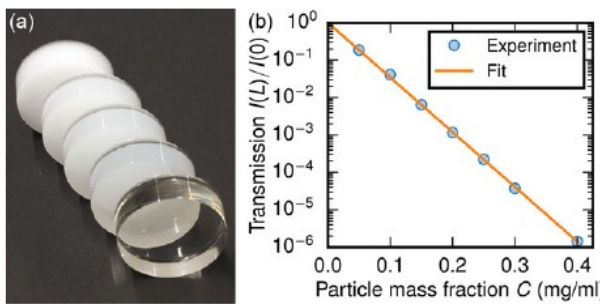


**Figure 2** Example measurement of the ballistic transmission through scattering media. (a) Photograph of test samples with a thickness of  $L = 1$  cm made of polydimethylsiloxane (PDMS) doped with  $\text{TiO}_2$  nanoparticles (245 nm mean diameter) and with different particle mass fractions. (b) Measured ballistic transmittance (plotted on a semilogarithmic scale) versus particle mass fraction  $C$  (blue circles). The fit according to Eq. (3) (solid orange line) yields a scattering mean free path of  $l_{\text{scat}} = 297(\mu\text{m mg/ml})/C$ .

Another important characteristic of an individual scattering event is the statistical distribution of scattering angles  $\theta$ , where  $\theta = 0$  corresponds to forward scattering and  $\theta = \pi$  to backward scattering. The distribution can be described by the statistical average over the corresponding cosine,

$$\langle \cos \theta \rangle = 2\pi \int_0^\pi \cos(\theta) p(\theta) \sin(\theta) d\theta, \quad (4)$$

with  $\langle \cos \theta \rangle \in [-1, 1]$ . Here,  $p(\theta)$  is the scattering phase function defined via

$$\int_{4\pi} p(\theta) d\Omega = 1, \quad (5)$$

i.e., it is the probability density that a photon is scattered into the solid angle  $d\Omega$  around  $\theta$  (assuming isotropic scatterers). The extremes are  $\langle \cos \theta \rangle = \pm 1$  for exclusively forward or backward scattering, respectively. Isotropic scattering or, more generally, scattering symmetric with respect to  $\theta = \pi/2$  such as Rayleigh scattering leads to  $\langle \cos \theta \rangle = 0$ . Microscopically, the scattering phase function  $p(\theta)$  can be calculated by the well-known Mie-scattering formulas [34, 35].

Consider parallel rays of unpolarized light impinging onto a scattering medium. After each ray has scattered just once, the direction of light rays is not yet fully randomized. The case  $\langle \cos \theta \rangle = 0$  is an exception. For all cases  $\langle \cos \theta \rangle \neq 0$ , it takes more than just a single scattering event on average to fully randomize the ray directions. The average distance that a photon propagates before its initial direction is fully randomized is the transport mean free path length,  $l_{\text{trans}}$ , given by [32, 38]

$$l_{\text{trans}} = l_{\text{scat}} \frac{1}{1 - \langle \cos \theta \rangle}. \quad (6)$$

For most scatterers, forward scattering dominates ( $\langle \cos \theta \rangle > 0$ ), resulting in a transport mean free path which is generally larger than the scattering mean free path,  $l_{\text{trans}} \geq l_{\text{scat}}$ .

### 2.1.1. The light-diffusion equation

In his original paper [39] introducing the diffusion equation, Adolf Fick considered massive particles. Speaking about particles makes the following discussions quite intuitive; hence, we formulate the light-diffusion equation for the local number density of (massless) photons  $n_{\text{phot}}(\vec{r})$ . Clearly, this wording does not mean that quantum aspects shall play any role at all. In fact, we will discuss the paths of photons just like rays of light (ignoring interference effects). Alternatively, we could formulate the diffusion equation for the electromagnetic energy density or for the fluence [32].

Without any absorption or loss, the total number of photons is conserved, which can be expressed via the continuity equation

$$\vec{\nabla} \cdot \vec{i} + \frac{\partial n_{\text{phot}}}{\partial t} = 0. \quad (7)$$

Here,  $\vec{i}$  is the local photon current density vector (with unit  $\text{m}^{-2}\text{s}^{-1}$ ) and  $n_{\text{phot}}$  the photon number density (with unit  $\text{m}^{-3}$ ). Finite loss of photons can be described via the absorption mean free path length  $l_{\text{abs}}$  and the energy velocity  $v_e$  of light or, alternatively, via a finite photon lifetime  $\tau = l_{\text{abs}}/v_e$ :

$$\vec{\nabla} \cdot \vec{i} + \frac{\partial n_{\text{phot}}}{\partial t} = -\frac{v_e n_{\text{phot}}}{l_{\text{abs}}} = -\frac{n_{\text{phot}}}{\tau}. \quad (8)$$

In a nearly dispersionless medium, the energy velocity at a certain wavelength is simply given by the phase velocity and thus by the vacuum speed of light  $c_0$  divided by the refractive index  $n$  of the background medium, i.e.,  $v_e = c_0/n$ . Solely by analogy to Fourier's equation of heat conduction, Adolf Fick made the *ad-hoc* ansatz today known as Fick's first law

$$\vec{i} = -D \vec{\nabla} n_{\text{phot}}, \quad (9)$$

with the diffusivity  $D$  (with unit  $\text{m}^2 \text{s}^{-1}$ ). Inserting this ansatz into Eq. (8) leads to the diffusion equation

$$\vec{\nabla} \cdot (D \vec{\nabla} n_{\text{phot}}) - \frac{\partial n_{\text{phot}}}{\partial t} = \frac{n_{\text{phot}}}{\tau}. \quad (10)$$

The diffusion equation can also be derived more rigorously from the radiative transport equation [32, 40, 41], leading to the diffusivity given by

$$D = \frac{1}{3} v_e l_{\text{trans}}. \quad (11)$$

The formal derivation of the diffusion equation requires two simplifying assumptions on the transport of light in

scattering media (namely on the radiance and the flux vector) [32]. These assumptions translate to the following set of rule-of-thumb conditions that need to be fulfilled simultaneously for a description of light propagation in terms of the diffusion equation to be justified.

- The transport mean free path length is significantly smaller than the smallest extent of a homogeneously disordered region, i.e.,  $l_{\text{trans}} \leq 0.1 L$ .
- The transport mean free path length is significantly larger than the wavelength of light, i.e.,  $l_{\text{trans}} \geq 10 \lambda$ . Otherwise, effects of light localization can come into play [42–45].
- The absorption mean free path length is significantly larger than the scattering mean free path length, i.e.,  $l_{\text{abs}} \gg l_{\text{scat}}$ .
- Photons have travelled a total distance of at least  $4 \times l_{\text{trans}}$  before being detected.

From this list and Eq. (11), it becomes immediately clear that neither  $D = 0$  nor  $D = \infty$  is possible. This must be kept in mind in the context of the following section, where such extreme parameters do actually occur mathematically. For example, for a wavelength of  $\lambda = 500 \text{ nm}$  (green light) and a macroscopic system size of  $L = 5 \text{ cm}$ , one gets a possible range of  $l_{\text{trans}} \in [5 \mu\text{m}, 5 \text{ mm}]$ . The ratio of upper limit to lower limit translates into three orders of magnitude of dynamic range for the diffusivity, i.e.,  $D_{\max}/D_{\min} = 1000$ . We note in passing that for passive materials, negative diffusivities [46, 47] are not compatible with the second law of thermodynamics (whereas equivalent negative refractive indices in ballistic optics are possible [48, 49]).

To investigate whether the above list of conditions is actually met in a given experimental setting, one needs to determine the scattering, transport, and absorption mean free path lengths. Above, we have already discussed ballistic transmittance experiments as a robust means to determine the scattering mean free path length  $l_{\text{scat}}$ . To obtain the transport mean free path length  $l_{\text{trans}}$  or the proportional light diffusivity  $D$  according to Eq. (11), however, one needs to perform a diffusion experiment.

### 2.1.2. How to measure diffusivity and absorption

Conceptually, one can, for example, generate a point-like, ultra-short flash of light within a turbid medium and then follow the width of the distribution versus time. This time-dependent distribution is just the well-known Green's function of the diffusion equation for a fictitious infinitely extended medium. It is given by

$$n_{\text{phot}}(\vec{r}, t) = N \frac{1}{(4\pi Dt)^{3/2}} \exp\left(-\frac{r^2}{4Dt} - \frac{t}{\tau}\right), \quad (12)$$

with the total number of photons  $N$ . The width of the distribution  $\sqrt{4Dt}$  increases proportionally to the square root of the diffusivity and the square root of the observation time. Absorption according to a finite lifetime  $\tau$  does change the absolute value of the photon density, but turns out to not

influence the width versus time at all. After division by the total number of photons, Eq. (12) can also be interpreted as the probability-density distribution for a single photon.

Practically, however, the photon density *inside* the diffusive medium is rarely accessible experimentally. The quantity much more relevant for almost all experiments is the photon current density that is reflected or transmitted at the sample's actual interfaces to air or vacuum. For such interfaces, one must make an additional assumption connecting the photon density at the interface to the current density in the non-diffusive region outside. There are at least three qualitatively similar yet quantitatively different possibilities for this boundary condition which have been treated in the literature [50–52]. We shall use only one in this review, known as the partial current boundary condition: we assume that no diffusive light can re-enter the medium from the external non-scattering region. Diffusive-light flow directed towards the diffusive medium can thus only originate from reflections at the boundary (or from external light sources). The resulting boundary condition is

$$i_n(\vec{r}) = \frac{v_e}{2A} n_{\text{phot}}(\vec{r}) = K n_{\text{phot}}(\vec{r}), \quad (13)$$

where  $i_n$  is the normal component of the photon current density at a certain location  $\vec{r}$  within the interface just inside of the diffusive medium. The dimension-less coefficient  $A$  represents the effects of Fresnel reflections at the interface to the surrounding, and thus depends on the refractive-index mismatch at this interface. One might be tempted to assume that these Fresnel reflections are small and can be neglected. One should, however, be aware that many light rays hit the interface under angles that are far from normal incidence. This leads to a rather large reflectance for both s- and p-polarization of light. Light rays may even experience total internal reflection. The average over the incidence angle enters  $A$  via [32]

$$A(n) = \frac{1 + 3 \int_0^{\pi/2} R_F(n, \cos \theta) \cos^2 \theta \sin \theta d\theta}{1 - 2 \int_0^{\pi/2} R_F(n, \cos \theta) \cos \theta \sin \theta d\theta}, \quad (14)$$

with the Fresnel reflectivity  $R_F(n, \cos \theta)$  for unpolarized light and the refractive index  $n$  of the diffusive medium (assuming that  $n = 1$  outside). Above, we have further defined the photon-escape velocity  $K$ . For a refractive index  $n = 1$ ,  $A$  is unity and the escape velocity assumes its maximum value of  $K = c_0/2$ . Intuitively, the factor  $1/2$  stems from the fact that on average half of the photons are moving away from the interface.

Given this boundary condition, solutions for a diffusive cuboid with side lengths  $L_x$ ,  $L_y$ , and  $L_z$  along the three spatial directions can, of course, be obtained by direct numerical solving of the diffusion equation (Eq. (10)). We find it more elegant though to use closed analytical expressions that are available in the literature. The approach to obtain them [32, 53] is related to the concept of image charges in electrostatics [54]. In diffusion, one introduces an artificially extended periodic version of the problem. For the placement of image sources and sinks, we assume that the

gradient of the photon density outside of the cuboid remains constant and equal to the value on the physical boundary. Then, the photon density itself becomes zero at an extrapolated distance  $z_e = D/K$  from the boundary. After quite some mathematics, one obtains the cuboid's Green's function for the photon density [55]

$$\begin{aligned} n_{\text{phot}}(\vec{r}, t) &= N \frac{1}{(4\pi Dt)^{3/2}} \exp\left(-\frac{t}{\tau}\right) \times \sum_{l=-\infty}^{\infty} \left\{ \exp\left(-\frac{(x - x_{1l})^2}{4Dt}\right) \right. \\ &\quad \left. - \exp\left(-\frac{(x - x_{2l})^2}{4Dt}\right) \right\} \times \sum_{m=-\infty}^{\infty} \left\{ \exp\left(-\frac{(y - y_{1m})^2}{4Dt}\right) \right. \\ &\quad \left. - \exp\left(-\frac{(y - y_{2m})^2}{4Dt}\right) \right\} \times \sum_{n=-\infty}^{\infty} \left\{ \exp\left(-\frac{(z - z_{1n})^2}{4Dt}\right) \right. \\ &\quad \left. - \exp\left(-\frac{(z - z_{2n})^2}{4Dt}\right) \right\}. \end{aligned} \quad (15)$$

with the following positions of the mirror sources and sinks:

$$\begin{aligned} x_{1l} &= 2lL_x + 4lz_e + x_s, \\ x_{2l} &= 2lL_x + (4l - 2)z_e - x_s, \\ y_{1m} &= 2mL_y + 4mz_e + y_s, \\ y_{2m} &= 2mL_y + (4m - 2)z_e - y_s, \\ z_{1n} &= 2nL_z + 4nz_e + z_s, \\ z_{2n} &= 2nL_z + (4n - 2)z_e - z_s. \end{aligned} \quad (16)$$

Here,  $(x_s, y_s, z_s)$  are the coordinates of the real source inside the medium, with  $(0, 0, 0)$  representing the corner of the cuboid. The infinite summation usually converges quickly and can thus be truncated after only a few elements. As for the case of an infinite diffusive medium, the finite photon lifetime  $\tau$  merely leads to an overall exponential decay of the photon density in Eq. (15). It does not influence the spatial shape of the curves at all. Thus, photon diffusivity  $D$  and lifetime  $\tau$  decouple and can reliably and unambiguously be determined independently by comparison of the above formula with experimental data.

Figure 3 illustrates experiment and (after deconvolution of the detector response function) theory according to Eq. (15) for the transmission of red laser light through PDMS doped with titania nanoparticles, using a calculated photon-escape velocity of  $K = 3.63 \times 10^7$  m/s for a PDMS refractive index of  $n = 1.4$ . The comparison yields a photon lifetime of  $\tau = 10.5$  ns and a photon diffusivity of  $D = 1.19 \times 10^{-9}$  cm<sup>2</sup>/s for a particle mass fraction of 0.39 mg/ml. Again using the PDMS refractive index and Eq. (11), this translates into a transport mean free path length of  $l_{\text{trans}} = 1.67$  mm.

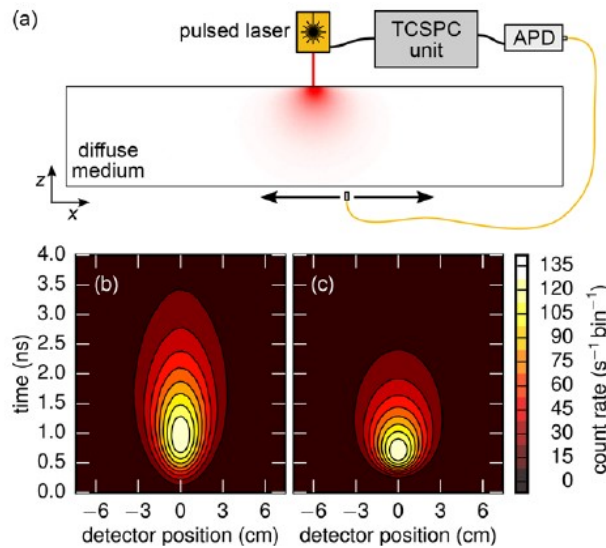


**Figure 3** (a) Scheme of an experiment to determine the parameters  $D$  and  $\tau$  of a diffuse medium according to Eq. (15). The time-resolved diffusive transmission of pulsed red laser light (pulse duration  $< 500$  ps) focused onto the diffusive medium is measured with an avalanche photodiode (APD) connected to a time-correlated single-photon-counting (TCSPC) unit. Spatial resolution is obtained by scanning the detection fiber along the  $x$ -axis. (b) Measurement result for a titania-doped PDMS cuboid (particle mass fraction  $C = 0.39$  mg/ml, mean particle diameter 245 nm) with dimensions  $L_x = 15$  cm,  $L_y = 8$  cm, and  $L_z = 3$  cm. For insufficient time resolution of the detector, the data need to be deconvoluted. Therefore, the analytical model given in Eq. (15) is first convolved with the measured instrument response function. The result is then fitted to the experimental data, with  $D$  and  $\tau$  as free parameters. For the input parameters  $K = 3.63 \times 10^7$  cm/s and PDMS refractive index  $n = 1.4$ , the deconvolution yields a photon lifetime of  $\tau = 10.5$  ns and a photon diffusivity of  $D = 1.19 \times 10^{-9}$  cm<sup>2</sup>/s. Panel (c) shows the non-convolved analytical result for these parameters.

### 2.1.3. Time scales and the stationary limit

Often, one would like to know whether the time derivative in the time-dependent diffusion equation is really important or whether one can neglect it, to justify the stationary or quasi-stationary limit (also see Sect. 3.1). Let us neglect losses for the moment, i.e.,  $\tau \rightarrow \infty$ . Still, broadly speaking, there is no such thing as a unique diffusive time constant (in the sense of an exponential decay) because the photon current density and hence the time scale depend on the local gradients. Large spatial gradients lead to short time scales. In general, the diffusive temporal decays are not even exponential. Thus, the concept of a diffusion time constant has to be taken with a grain of salt. For example, using the above Green's function for an infinite homogeneous lossless diffusive medium, one can calculate the time at which the average squared distance of photons from the excitation center equals  $L^2$  with some characteristic length

$L$  (e.g., the sample thickness) and call this time the diffusion time  $\tau_{\text{diff}}$  [56, 57]. One obtains the general form

$$\tau_{\text{diff}} = \frac{L^2}{2\xi D}, \quad (17)$$

with the dimensionless parameter  $\xi = 3$  in three dimensions,  $\xi = 2$  in two dimensions, and  $\xi = 1$  in one dimension.

What is the stationary light transmission (under stationary excitation) of the diffusive cuboid considered above? In this form, the question is not quite well defined because the light emission is not going to be homogeneous across the surface unless we consider the limit of a fictitiously infinitely extended slab, i.e.,  $L_x \rightarrow \infty$  and  $L_y \rightarrow \infty$ , while keeping  $L_z$  finite. We homogeneously illuminate the slab from one side along the  $z$ -direction. By translational symmetry along the  $x$ - and  $y$ -directions, the emerging photon current density vector on the downstream side has only a non-vanishing  $z$ -component (= normal component). Working out the mathematics with the ansatz  $n_{\text{phot}}(z) = a \exp(-\alpha z) + b \exp(+\alpha z)$  [58] and a constant incident light flux  $i_{\text{in}}$  leads us to the diffusive transmittance

$$T_{\text{diff}} = \frac{i_{\text{trans}}}{i_{\text{in}}} = \frac{2D\alpha K}{(D\alpha + K)^2 e^{+\alpha L_z} - (D\alpha - K)^2 e^{-\alpha L_z}}. \quad (18)$$

Here, we have introduced the effective absorption coefficient  $\alpha = 1/\sqrt{D\tau}$ . Its inverse can be interpreted as a diffusion length, which tells us how far photons make it on average within their lifetime. In principle, the parameters  $K$ ,  $D$ , and  $\tau$  can be obtained by comparing the measured diffusive transmittance with Eq. (18) upon varying  $L_z$  while fixing the concentration of scattering particles or upon varying the concentration of scattering particles while fixing  $L_z$ . The latter has been done experimentally in Ref. [58], but this procedure turns out to be much less robust than the procedure based on the cuboid Green's function of the problem described above.

In the limit of negligible absorption, i.e., for  $\tau \rightarrow \infty$  at finite  $D$  and hence  $\alpha \rightarrow 0$ , Eq. (18) simplifies to

$$T_{\text{diff}} = \frac{1}{2 + \frac{KL_z}{D}}. \quad (19)$$

It becomes obvious that the escape velocity  $K$  has a concrete influence on important measurable results. In the mathematical limit of  $K \rightarrow 0$ , which corresponds to near-unity Fresnel reflections at the interfaces, the diffusive transmittance approaches the limit of  $T_{\text{diff}} = 1/2 = 50\%$ . Intuitively, the transmittance cannot exceed this value because the photon directions get completely randomized inside a diffusive medium. This limit is reached for negligible gradient of the photon density ( $KL_z/D \rightarrow 0$ ). For finite gradients, the forward-backward symmetry is broken and the diffuse transmittance is always below this value. For large slab

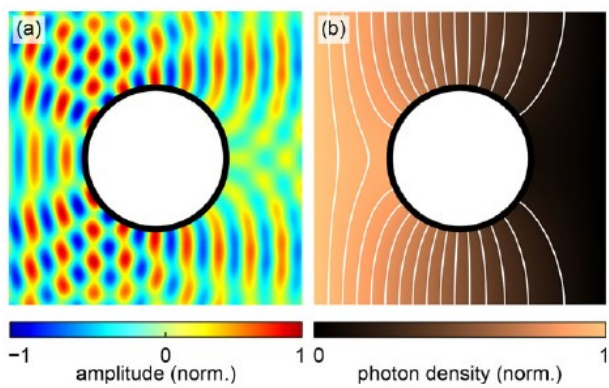


**Figure 4** Qualitative comparison between wave optics and diffusive optics. (a) A plane wave in vacuum (amplitude color coded) impinging from the left onto a metallic ring is heavily disturbed and shows reflection, shadowing, and interference. (b) A diffusive light current (photon density color coded) impinging from the left onto an isolating zero-diffusivity ring shows much less pronounced effects, demonstrating the qualitative difference between wave optics and diffusive optics. The white curves are equidistant isolines of the photon density.

thicknesses  $L_z$ , i.e., for  $KL_z/D \gg 2$ , the diffusive transmittance behaves as

$$T_{\text{diff}} \approx \frac{D}{KL_z} \propto \frac{1}{L_z}. \quad (20)$$

It should not surprise us that the transmittance decreases inversely with the slab thickness  $L_z$  (rather than following Beer's exponential law). This behavior is analogous to Ohm's law for electrical conduction, where the electrical current density decreases inversely with the length of a metal wire (or the thickness of a metal slab) for a fixed voltage across the ends of the wire. Likewise, the current proportionally increases with increasing electrical conductivity of the metal  $\sigma$ —which is analogous to the proportional increase of the transmittance versus diffusivity  $D$  here. In fact, in the regime of Boltzmann transport [59], the electrons in a metal perform a diffusive random walk just like the photons we discuss here. We will come back to this close physical as well as mathematical analogy between electrical transport and diffusive light in the following section.

#### 2.1.4. Comparison to ballistic transport and significance of coherence

Broadly speaking, the above expression for the diffusive transmittance (Eq. (19)) of a homogeneous slab in vacuum can be seen as the diffusive counterpart of a three-dimensional Fabry-Pérot resonator in ballistic wave optics. We do emphasize, however, that interference of light and all aspects resulting from that like, e.g., diffraction are absent on the level of the above diffusion equation for light. To illustrate this fact, Fig. 4 compares two situations. On the

left-hand side, an optical plane wave in vacuum impinges from the left onto a metallic ring, which isolates its interior from its exterior. Obviously, the wave is strongly distorted. On the right-hand side, a diffusive light current in a homogeneous diffusive medium impinges from the left onto a ring with zero diffusivity, which also isolates its interior from its exterior. The resulting behavior is very different. Nevertheless, one can also see similarities when comparing the behavior of the phase fronts with the white isolines of the photon density.

Finally, we note that effects of interference of light waves can still be observed in specific experiments on strongly scattering optical media—even if all conditions for the diffusion equation to be valid in the above list are fulfilled: sending a monochromatic laser beam with sufficiently large coherence length onto a diffusive slab or cuboid leads to the well-known phenomenon of laser speckles [60]. These speckles can no longer be seen with the naked human eye if the scattering particles move with time or if an incoherent (e.g., broadband) laser light source is used. Amazingly, the wave nature of light can also influence the measured diffusive transmittance [61–63]. Suppose we do not illuminate a slab with a homogeneous incident intensity (as assumed above) but rather with an inhomogeneous pattern which varies on the spatial scale of the wavelength of light. We can classify all possible two-dimensional patterns by expanding them into some sort of complete set of orthogonal modes, similar to the electromagnetic modes of a laser cavity. It has been shown theoretically as well as experimentally that the different input modes lead to different total light powers being transmitted across the downstream facet of the slab or cuboid, i.e., to different diffusive transmittances. Some modes called “open modes” can lead to a transmittance that is larger by factors than that of others called “dark modes” [62]. The statistics of these modes has been studied in detail [61]. In this review, we shall not consider such somewhat special (although quite interesting) illumination conditions any further.

## 2.2. Anisotropic diffusion and laminates

So far, we have assumed that the medium in which photons propagate diffusively is locally isotropic in an average sense. This need not be the case. In fact, anisotropies are key to molding the flow of photons as we wish because they will allow us to guide the flow of photons into particular directions. Let us consider the stationary ( $\partial/\partial t = 0$ ) version of Eq. (10) for vanishing absorption ( $\tau \rightarrow \infty$ ). For a homogeneous and isotropic diffusive medium, this leads us to

$$\vec{\nabla} \cdot (D \vec{\nabla} n_{\text{phot}}) = 0. \quad (21)$$

This equation has the same mathematical form as the stationary electric current conduction equation, which can be derived from the first Maxwell equation without external charges  $\vec{\nabla} \cdot \vec{D} = 0$ . With  $\vec{D} = \epsilon_0 \epsilon \vec{E}$ ,  $\vec{E} = -\vec{\nabla} \varphi$  with the

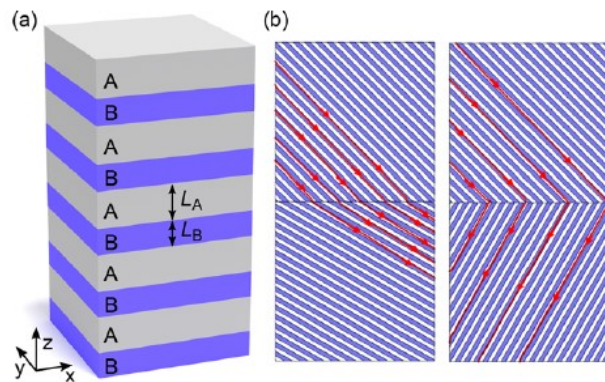


**Figure 5** (a) Illustration of an anisotropic laminate metamaterial composed of two different constituent materials A and B with diffusivities  $D_A$  and  $D_B$ . (b) Calculated streamlines of the heat flow or, mathematically equivalent, of the flow of photons for two different arrangements of laminates under an angle. In the left-hand sub-panel, “positive refraction” occurs, in the right-hand sub-panel “negative refraction”. Panel (b) reprinted with permission from Ref. [64]. Copyright 2014, AIP Publishing LLC.

electrostatic potential  $\varphi$ , and Ohm’s law for the electrical current density vector  $\vec{j} = \sigma \vec{E}$  with the electrical conductivity  $\sigma$ , this leads to

$$\vec{\nabla} \cdot (\sigma \vec{\nabla} \varphi) = 0 \quad (22)$$

(or to the electrostatic equation  $\vec{\nabla} \cdot (\epsilon \vec{\nabla} \varphi) = 0$  with the electric permittivity  $\epsilon$ ). Obviously, the photon density  $n_{\text{phot}}$  is the counterpart of the electrostatic potential  $\varphi$  and the photon diffusivity  $D$  is the counterpart of the electric conductivity  $\sigma$ . It thus often helps if one merely replaces the words “photon diffusivity” by “photon conductivity” to get the right intuition for a problem.

Next, let us consider a stack of layers A and B with thicknesses  $L_A$  and  $L_B$  and with alternating high and low diffusivities  $D_A$  and  $D_B$  as depicted in Fig. 5 (a). As an extreme case, one of the layers could exhibit  $D_A = 0$ . In this case, it is immediately clear that the photon current normal to the layers is zero, whereas the current can be finite within the plane of the layers. This effective anisotropy can be cast into an effective diffusivity tensor  $\vec{D}$ . In the electrical case, the problem boils down to parallel (in-plane) and serial (normal to plane) circuits of resistors. By translation, this leads to the diffusivity tensor

$$\vec{D} = \begin{pmatrix} D_{xx} & 0 & 0 \\ 0 & D_{yy} & 0 \\ 0 & 0 & D_{zz} \end{pmatrix}. \quad (23)$$

Its elements are given by the relations [65]

$$D_{xx} = D_{yy} = \frac{L_A D_A + L_B D_B}{L_A + L_B} \quad (24)$$

and

$$\frac{L_A + L_B}{D_{zz}} = \frac{L_A}{D_A} + \frac{L_B}{D_B}. \quad (25)$$

Altogether, by replacing  $D \rightarrow \overset{\leftrightarrow}{D}$ , via  $\vec{i} = -\overset{\leftrightarrow}{D} \vec{\nabla} n_{\text{phot}}$ , this leads us to the generalized version of the lossless stationary diffusion equation

$$\vec{\nabla} \cdot (\overset{\leftrightarrow}{D} \vec{\nabla} n_{\text{phot}}) = 0. \quad (26)$$

For example, if  $D_{xx} = D_{yy} \gg D_{zz}$ , the photon current will mainly flow within the  $xy$ -plane no matter how large the gradient along the  $z$ -direction is. This means that the lamination allows us to force the photons to flow along certain directions. An example is shown in Fig. 5(b), where we consider an interface between two high-contrast laminates, the axes of which include an angle. Clearly, the direction of flow changes at the interface—equivalent to refraction in ballistic optics. The situation depicted in the right-hand panel of (b) is the counterpart of negative refraction [66].

Mathematically, we can even consider the limits  $L_A \rightarrow 0$  and  $L_B \rightarrow 0$ . This means that we can construct arbitrary spatial tensor distributions  $\overset{\leftrightarrow}{D} = \overset{\leftrightarrow}{D}(\vec{r})$  by tailoring the local lamination direction and the local diffusivities of the laminate layers and thereby mold the diffusive flow of photons along any path, as we wish.

The mathematical limits  $L_A \rightarrow 0$  and  $L_B \rightarrow 0$ , however, require some caution for the case of light diffusion. We eventually violate the set of conditions discussed above for the validity of the diffusion equation because the layer thicknesses  $L$  will no longer be much larger than the local transport mean free path lengths  $l_{\text{trans}}$ . Mathematically, we could first consider the limit of  $l_{\text{trans}} \rightarrow 0$  and hence  $D \rightarrow 0$  for all layers, but this means that we would deal with essentially optically opaque systems (see Eq. (19) above for the diffusive transmittance), which, experimentally, are not very interesting and relevant at all. Furthermore, even localization of light [43–45] would come into play at some point. For finite concentrations of scattering particles and hence finite photon diffusivities, it simply does not make sense to reduce the laminate layer thicknesses below a certain point. This aspect must be kept in mind in regard to the findings of the following sections. It means that any continuous distribution of the diffusivity will be discretized into piecewise-homogeneous regions.

Apart from these limitations, we have seen that the concept of laminates allows us to mold the flow of light via anisotropic diffusion, which can be described mathematically by a local diffusivity tensor. A laminate can be seen as an artificial material or “metamaterial” because its effective properties go beyond (“meta”) those of the constituent layers: the metamaterial yields anisotropic properties from isotropic constituents.

## 2.3. Using transformations for design

In ordinary ballistic (linear) optics, optical systems and devices are often based on tailored spatial distributions of the refractive index  $n(\vec{r})$  (e.g., in lens systems, waveguides, optical fibers, or dielectric mirrors) or of the refractive-index tensor  $\overset{\leftrightarrow}{n}(\vec{r})$  (e.g., in birefringent polarizers, half-wave plates, or Wollaston prisms). Can we proceed likewise in the regime of diffusive optics and tailor the local diffusivity  $D(\vec{r})$  or the diffusivity tensor  $\overset{\leftrightarrow}{D}(\vec{r})$ ? The discussion in the previous section has suggested that the answer is yes. But how can we rationally design the distribution  $\overset{\leftrightarrow}{D}(\vec{r})$  to achieve a given function or behavior? In general, this question refers to a difficult inverse problem. Spatial transformations can help us to solve it in an intuitive manner.

Consider a general spatial (coordinate) transformation

$$\vec{r} \rightarrow \vec{r}' = \vec{r}'(\vec{r}). \quad (27)$$

For example, this transformation can correspond to a local stretch or compression of space. Such a transformation can be visualized by drawing a rectangular grid of lines onto a flexible rubber sheet. If you want the lines to go along different paths, you can simply pull on the sheet or compress it in other regions. If we can somehow make photons actually flow along these modified paths, we have succeeded in our goal.

Let us note in passing that we have put the word “coordinate” above into parentheses because the transformations we have in mind are not actually coordinate transformations, in the sense that we describe the same physical situation merely in a different coordinate system (such as transforming from Cartesian to spherical coordinates when solving the Schrödinger equation of the hydrogen atom). Nevertheless, the transformations we discuss here are often referred to as coordinate transformations in the literature anyway. Other authors have introduced the notion of “corporeal” transformations [67] to make them distinct from coordinate transformations.

Before we address the general case mathematically, let us consider a very simple example, namely a global stretching along all directions by a constant factor  $s = 10$ , i.e.,  $\vec{r} \rightarrow \vec{r}' = s\vec{r}$ . We insert this transformation into Eq. (10), having in mind that the diffusivity herein could actually be spatially varying in some manner, i.e.,  $D = D(\vec{r})$ , and so could the photon lifetime  $\tau = \tau(\vec{r})$ . We look at the original behavior and that after the transformation on a computer monitor. After the transformation, the flow of light is simply taking place in the same shape and on the same time scale but on a 10 times bigger spatial scale. Can we map this fictitious transformation onto a new diffusivity distribution such that the flow of light *actually* takes place on a 10 times bigger spatial scale? With  $\vec{\nabla} \rightarrow \vec{\nabla}' = \vec{\nabla}/s$ , the two spatial gradients on the left-hand side yield a multiplicative factor of  $1/s^2$ . If we replace the diffusivity  $D \rightarrow D' = Ds^2$ , the time according to  $t \rightarrow t' = ts^2$ , and the photon lifetime via  $\tau \rightarrow \tau' = \tau s^2$ , the stretching factor  $s$  drops completely

out of the equation. However, the behavior now takes place on a different time scale  $t' \neq t$ , which means that we have not completely achieved our goal. This problem obviously disappears for the stationary limit, in which case we have successfully mapped our global 10-fold spatial stretching factor onto a 100 times larger diffusivity and onto a 100 times larger photon lifetime.

Mathematically speaking, by discussing this counter-example for transient diffusion, we have proven that the time-dependent diffusion equation is not form invariant under general spatial transformations. The issue is simply that we have no pre-factor in front of the temporal derivative in Eq. (10) by which we could absorb the factor  $s^2$  other than shifting it into time itself. This problem does not, for example, arise in the time-dependent heat conduction equation [68], in Maxwell's equations [12], or in the acoustic wave equation [69].

Is the stationary diffusion equation form invariant under *general* spatial transformations as in Eq. (27) beyond this special simple example? We start with the important mathematical identity [70]

$$\vec{\nabla} \cdot \vec{\nabla} \rightarrow \det(\overset{\leftrightarrow}{J}) \vec{\nabla} \cdot \left( \overset{\leftrightarrow}{J} \overset{\leftrightarrow}{J}^T \frac{1}{\det(\overset{\leftrightarrow}{J})} \vec{\nabla}' \right), \quad (28)$$

with the Jacobian matrix  $\overset{\leftrightarrow}{J}$ , the elements of which are given by

$$(\overset{\leftrightarrow}{J})_{ij} = \frac{\partial x'_i}{\partial x_j}. \quad (29)$$

The superscript "T" refers to the transposed matrix. Inserting this identity into the stationary version of the diffusion equation (Eq. (10)),

$$\vec{\nabla} \cdot (D \vec{\nabla} n_{\text{phot}}) = \frac{n_{\text{phot}}}{\tau}, \quad (30)$$

allows us to write

$$\vec{\nabla}' \cdot (\overset{\leftrightarrow}{D}' \vec{\nabla}' n_{\text{phot}}) = \frac{n_{\text{phot}}}{\tau'}, \quad (31)$$

with the transformed spatially dependent diffusivity tensor

$$\overset{\leftrightarrow}{D}' = D \overset{\leftrightarrow}{J} \overset{\leftrightarrow}{J}^T \frac{1}{\det(\overset{\leftrightarrow}{J})} \quad (32)$$

and the transformed spatially dependent photon lifetime

$$\tau' = \tau \det(\overset{\leftrightarrow}{J}). \quad (33)$$

For negligible losses or infinitely large photon lifetime, the right-hand side of the diffusion equation is simply zero and need not be transformed. Notably, the transformed equation

(31) has the same mathematical form as the original equation, i.e., the stationary diffusion equation is form invariant under general spatial transformations. Equations (32) and (33) are recipes telling us how the material parameters have to be transformed to mimic the fictitious transformation. Notably, finite losses do not necessarily spoil the approach for light diffusion.

Now that we have the desired design tool at hand, we will discuss a stationary invisibility cloak as a first example for transformation-based designs. More examples will be discussed in detail in Sect. 2.5.

The first example is the two-dimensional transformation of a (singular and thus invisible) point to a circle of radius  $R_1$  (or the other way around), which is expressed best in polar coordinates with radial coordinate  $r$  and azimuthal angle  $\theta$ . There are infinitely many possibilities [71] to accomplish this transformation. The simplest one is linear [12] and given by

$$r \rightarrow r'(r, \theta) = R_1 + \frac{R_2 - R_1}{R_2} r, \\ \theta \rightarrow \theta'(r, \theta) = \theta \quad (34)$$

for  $0 < r < R_2 > R_1$  and no transformation for  $r \geq R_2$ . Obviously, the transformation is continuous at  $r = R_2$ . To insert this transformation into our recipe, one needs to switch back and forth by coordinate transformations between Cartesian coordinates and polar coordinates. This makes the calculation quite tedious. Starting with a constant and isotropic diffusivity  $D_0$ , i.e., a homogeneous diffusive system, the resulting non-zero tensor components of the photon diffusivity tensor in polar coordinates can be approximated by [68]

$$D'_{rr}(r, \theta) \approx D_0 \left( \frac{R_2}{R_2 - R_1} \right)^2 \left( \frac{r - R_1}{r} \right)^2 \leq D_0 \quad (35)$$

and

$$D'_{\theta\theta}(r, \theta) \approx D_0 \left( \frac{R_2}{R_2 - R_1} \right)^2 = \text{const.} > D_0. \quad (36)$$

We get an anisotropic behavior with a large diffusivity in the azimuthal ( $\theta$ ) direction and a small diffusivity in the radial ( $r$ ) direction. Near the inner radius  $R_1$ , the radial component even tends to zero, preventing photons from diffusing into the core of this invisibility cloak.

We can also once again exploit the close analogy to electrical conduction (see above) to get a better intuition for this example. Consider the discrete resistor network shown in Fig. 6. It can be seen as a model for an isotropic and homogeneous conductor. Upon performing the described transformation (Eq. (34)) on the crossing points of the lattice, one gets an inhomogeneous and anisotropic network. Yet, as all resistors and all connections between them are still the same, the two different networks will be indistinguishable for resistance measurements from the outside, i.e., at the edges. This means that we have made the central hole

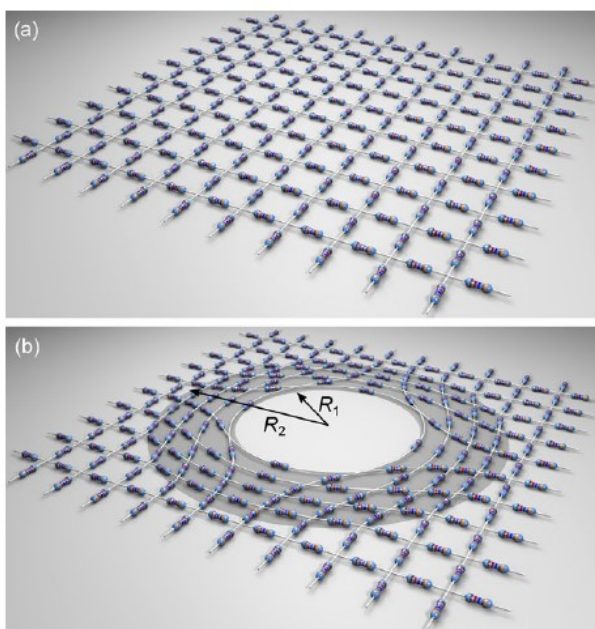


**Figure 6** Illustration of transformation physics for the example of electrical conduction. (a) A rectangular grid of identical resistors represents a homogeneous, isotropically conducting medium. (b) Transforming this discrete grid results in a mere re-arrangement of the resistors (assuming that the wires have zero resistance). With stationary resistance measurements outside of  $R_2$ , it is impossible to distinguish the two cases. The different radial and azimuthal densities of resistors connected in parallel indicate the anisotropy of the transformed structure. Reproduced from Ref. [72].

invisible with respect to electrical conduction. One can even see the local anisotropies which we have quoted above: along the azimuthal direction, we have more resistors in parallel per unit area near the inner radius than in the original lattice. This means that the local azimuthal conductivity (diffusivity) has gone up. In contrast, in the radial direction, we have fewer resistors in parallel and more resistors in serial per unit area compared to the square lattice. Hence, the local radial conductivity (diffusivity) has decreased in the transformed lattice with respect to the original one.

Figure 7 shows current streamlines of photon flow obtained from numerical calculations based on the stationary lossless diffusion equation for the homogeneous case and the transformed case, i.e., for the invisibility cloak—for the same geometrical parameters  $R_1$  and  $R_2$  as the resistor network in Fig. 6.

Finally, we point out that the transformation approach outlined in this section also has immediate implications for diffuse optical tomography [73, 74]. In tomography [75], the aim is to obtain sectional images of the interior of some object by measurements from the outside. Example applications are breast cancer imaging [76, 77] or the monitoring of cerebral hemodynamics (the fluid dynamics of blood flow inside the brain) [78, 79]. Some diffuse-optical-tomography approaches are based on continuous-wave illumination with lasers [80]; others use intensity-modulated or pulsed lasers and time-resolved detection [81–84]. The possibility of sta-

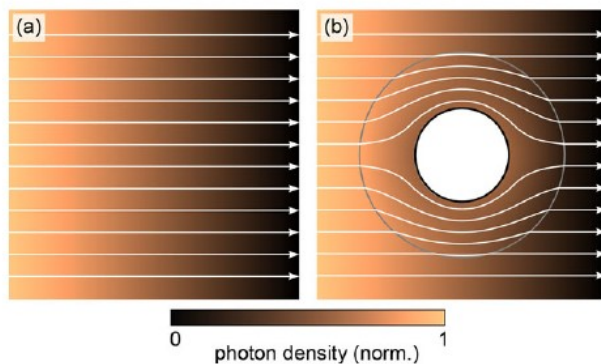


**Figure 7** Numerically calculated photon current streamlines based on the stationary lossless diffusion equation. (a) A homogeneous medium shows straight, undisturbed photon flow. (b) An invisibility cloak implementing the transformation given in Eq. (34) leaves the photon flux undisturbed outside of the cloak. The cloak's extent is indicated by the gray circle.

tionary invisibility cloaking means that one cannot distinguish a homogeneous diffusive medium from one with an obstacle and a cloak around it. This non-uniqueness of the tomography problem was previously proven mathematically [85]. For the equivalent electrical problem, it becomes rather obvious when comparing the two resistor networks shown in Fig. 6. An infinite number of additional examples for material distributions that are actually different but which are completely indistinguishable from the outside in terms of diffuse light can be generated by other transformations which are compact, i.e., which are limited to a finite region in space. In contrast, conformal transformations [13, 20, 86] are transformations which are unavoidably infinitely extended in space. They preserve local angles and hence lead to locally isotropic photon diffusivities. This means that the diffusive-optical-tomography problem becomes unique again also in the stationary case if we exclude the possibility of locally anisotropic diffusion.

Is the diffuse-optical-tomography approach unique under *transient* conditions? We have seen above that the transient light-diffusion equation is not form invariant under spatial transformations. This means that one cannot transfer our reasoning for the stationary case to the transient case. Hence, the transient diffuse-optical-tomography problem has a unique solution. We will discuss experiments under transient conditions in Sect. 3.2.

## 2.4. Core–shell cloaking structures

### 2.4.1. Single-shell cloaking structures

On the basis of the preceding section, we are now in a position to design distributions of generally inhomogeneous and anisotropic photon diffusivities. These can be realized by using the laminates discussed in Sect. 2.2. There, however, we have also seen that the individual laminate layers need to have a certain minimum thickness in order to stay within the range of validity of a description in terms of photon

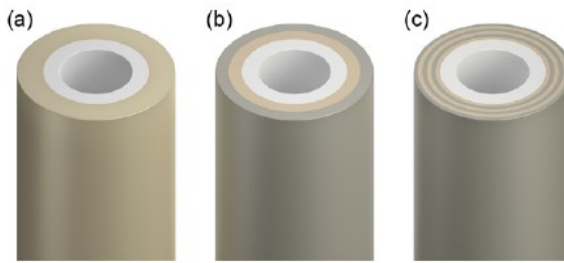


**Figure 8** Examples of cylindrical invisibility cloaks composed of increasingly many layers. (a) Core–shell structure with a low-diffusivity core and a high-diffusivity shell. (b) Structure with an additional low-diffusivity shell. (c) Core surrounded by six shells with alternatingly high and low diffusivity.

diffusion. Thus, we need to discretize the diffusivity distribution. The present as well as the following section address this problem for the example of an invisibility cloak. In essence, we first use the crudest possible approximation, namely just a single period of a laminate, i.e., one low-diffusivity layer and one high-diffusivity layer embedded in a surrounding. The following section then asks how quickly the behavior converges towards the ideal of transformation optics if we allow for successively more and more layers. The three panels of Fig. 8 illustrate this transition.

We again consider a homogeneous surrounding with a constant scalar diffusivity  $D_0$ . We have seen that for an invisibility cloak, the radial component of the photon diffusivity needs to converge to zero at the inner radius  $R_1$ . Hence, we start with a circle of radius  $R_1$  and diffusivity  $D_1 = 0$  within. This circle is just a diffusive reflector of light because the normal component of the photon current vector with respect to an interface is zero. We can also think of it as an isolator for photons analogous to an electrical isolator. For strictly zero diffusivity, we can cut out the central part of that circle because light does not propagate in there anyway. Arbitrary objects can be located within this void. Next, we surround this “core” by a single “shell” layer, such that core and shell together can be seen as one period of a laminate metamaterial. The shell shall have the radius  $R_2$  and the constant diffusivity  $D_2$ . How can we choose these two parameters such that the core–shell cloak is indistinguishable from the homogeneous surrounding?

This problem has been solved mathematically many times in the literature. The first solution was provided by Kerner in 1956 in a paper discussing “coated grains” [87]. A comprehensive review of the corresponding following literature can be found in Ref. [65]. The problem can be treated analytically if the gradient of the photon density in the background medium is assumed to be constant across the structure. This situation corresponds to homogeneous illumination as well as negligible absorption. To obtain invisibility under this condition, the shell parameters must obey the relation

$$\frac{R_2}{R_1} = \sqrt[3]{\frac{D_2 + D_0}{D_2 - D_0}} \Leftrightarrow \frac{D_2}{D_0} = \frac{R_2^3 + R_1^3}{R_2^3 - R_1^3}. \quad (37)$$

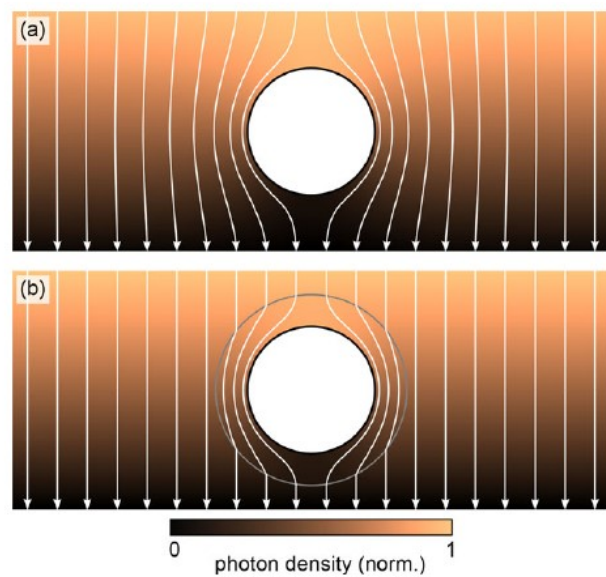


**Figure 9** Calculated photon-density distribution (color coded) with superimposed photon current streamlines (white arrows) for two-dimensional core–shell structures embedded in a finite slab that is homogeneously illuminated from above. (a) A zero-diffusivity core (the “obstacle”) disturbs the photon flow through the homogeneous surrounding (diffusivity  $D_0$ ), leading to distorted streamlines. (b) A core coated with a single homogeneous shell with the right diffusivity according to Eq. (37) makes the core–shell structure (the “cloak”) invisible and leads to a photon flow as if only a homogeneous medium (the “reference”) was there.

This solution refers to a two-dimensional circular or to a cylindrical geometry. The solution for an analogous three-dimensional spherical geometry is given by

$$\frac{R_2}{R_1} = \sqrt[3]{\frac{D_2 + D_0/2}{D_2 - D_0}} \Leftrightarrow \frac{D_2}{D_0} = \frac{R_2^3 + R_1^3/2}{R_2^3 - R_1^3}. \quad (38)$$

Obviously, the required contrast  $D_2/D_0$  diverges in both cases if the shell becomes thinner and thinner, i.e., for the limit  $R_2 \rightarrow R_1$  (see denominators on the right-hand sides). However, even for rather thin shells with  $R_2/R_1 = 1.25$ , the contrast stays moderate with  $D_2/D_0 \approx 4.6$  ( $D_2/D_0 \approx 2.6$ ) in two (three) dimensions. Note that the assumed mathematical value of  $D_1 = 0$  is not actually accessible experimentally for light diffusion (see Sect. 2.1). However, the above results stay meaningful in an approximate sense for  $D_1 \ll D_0 < D_2$ , which can be achieved experimentally.

Figure 9 illustrates the two-dimensional case by numerical solutions for a slab with finite thickness with the boundary conditions as discussed in Sect. 2.1. We compare the “obstacle”, i.e., the uncoated zero-diffusivity core embedded in the surrounding, with the “cloak”, where the core is coated by the additional high-diffusivity shell. We call the homogeneous case without core or shell the “reference”. (We will use this nomenclature throughout the rest of this article.) It becomes clear that under homogeneous

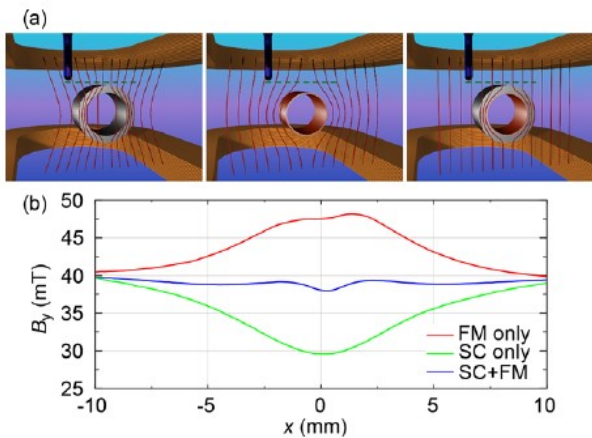


**Figure 10** Magnetostatics is described by the equation  $\vec{\nabla} \cdot (\mu \vec{\nabla} \Phi) = 0$ , with relative magnetic permeability  $\mu$  and scalar magnetic potential  $\Phi$ . This equation is equivalent to the stationary light-diffusion equation; see Eq. (21). (a) Scheme of the experiment with superconducting (SC) core with  $\mu = 0$  only, with ferromagnetic (FM) shell with  $\mu > 1$  only, and for the core–shell (SC + FM) structure, all in air with  $\mu = 1$ . The Helmholtz coils at the bottom and top generate a rather homogeneous magnetic field along the vertical  $y$ -direction. (b) Corresponding measurements of the magnetic field along the dashed straight line in (a) show a fairly constant magnetic field for the core–shell case, evidencing good cloaking. From Ref. [89]. Reprinted with permission from AAAS.

illumination, simple core–shell cloaks work perfectly. Amazingly, they also work reasonably well for spatially inhomogeneous illumination. We will numerically address this aspect, which has also been found for the mathematically analogous case of stationary heat conduction [88], in the following section as well as experimentally in Sect. 3.1.1. Experimental results for the analogue of a magnetostatic core–shell cloak are shown in Fig. 10 [89].

Note that we have assumed zero photon losses throughout this section. We will show (imperfect) results including realistic losses ( $\tau \neq \infty$ ) when comparing solutions of the diffusion equation to experiments in Sect. 3.1.1. Furthermore, we have assumed stationary conditions in this section. Results for core–shell cloaks under transient conditions will be presented in Sect. 3.2.

#### 2.4.2. Multiple-shell cloaking structures

In this section, we investigate the transition from the simple cloaks with only a single shell layer of the preceding section to structures closer to the coordinate-transformation cloaks as introduced in Sect. 2.3. By defining a suitable figure of merit, we show that going from two to three layers in total (i.e., going from core plus one shell to core plus two shells) yields a huge improvement, such that the performance is already extremely close to that of an ideal cloak.

As noted before, core–shell cloaking according to Eqs. (37) and (38) is perfect under homogeneous illumination

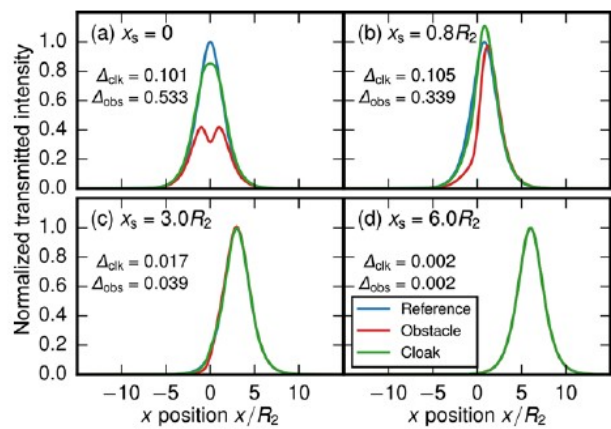


**Figure 11** Calculated transmitted intensity profiles for core–shell structures as shown in Fig. 9 for point-like Gaussian illumination (full width at half maximum of  $0.04 R_2$ ) at different positions  $x_s$ . For source positions close to the sample center, obstacle as well as cloak show significant deviations from the homogeneous reference (panels (a) and (b)). Further away, both obstacle and cloak converge to the reference behavior (panels (c) and (d)). The average relative standard deviations  $\Delta$  according to Eq. (39) are given with respect to the reference curve. Parameters are  $R_1 = 0.8$  cm,  $R_2 = 1.5 R_1$ ,  $L_z = 2.5 R_2$ ,  $D_1 = 0$ ,  $D_0 = 1.19 \times 10^9$  cm $^2$ /s,  $D_2 = 2.6 D_0$ , and  $K = 3.63 \times 10^9$  cm/s.

and without losses. To quantify the cloaking quality for inhomogeneous illumination, we need a suitable unambiguous figure of merit. Inspired by Ref. [90], we start from the average relative standard deviation,  $\Delta$ , of the cloak with respect to the homogeneous surrounding. Here, “average” refers to an average with respect to image pixels. Precisely, we define the dimensionless quantity

$$\Delta = \frac{\sqrt{\sum_i (n_{\text{phot},i} - n_{\text{phot},i}^0)^2}}{\sqrt{\sum_i (n_{\text{phot},i}^0)^2}}, \quad (39)$$

where  $n_{\text{phot},i}$  is the photon density for the cloak or for the obstacle case, respectively, in pixel  $i$  of an image plane and  $n_{\text{phot},i}^0$  is the corresponding value for the reference case—all for a given illumination condition. The sums run over all image pixels or over a selected range thereof, because it is not meaningful to involve pixels that are too far away from the core–shell structure. These pixels are not influenced by the structure, hence leading to  $\Delta \rightarrow 0$  even for an obstacle without cloak. As in the previous section, we discuss cylindrical, i.e., effectively two-dimensional, cloaks, for which the numerical calculations are much faster. The procedure can analogously be applied to three dimensions as well. In three dimensions, the to-be-cloaked deviations are similar but actually less pronounced [58].

Figure 11 shows calculated transmittance profiles of such two-dimensional structures illuminated by a Gaussian point-like source for selected source positions, demonstrating that for source positions close to the core–shell

structure, the cloak's behavior deviates significantly from that of the homogeneous reference. To study the cloaking quality for all possible non-homogeneous illumination conditions, we represent an arbitrary illumination by a superposition of many such point-like illuminations. This is meaningful because the diffusion equation is linear. We then average  $\Delta$  (which is already an average with respect to the image points) over all relevant point-like illuminations to obtain an averaged relative average standard deviation  $\langle \Delta \rangle$ . To optimize the cloaking performance of a given structure under inhomogeneous illumination, we minimize  $\langle \Delta \rangle$  in a numerical optimization loop with the diffusivity in each shell as the independent variable. To obtain meaningful results, we fix the outer radius of the core  $R_1$  as well as the outer radius of the outermost shell ( $R_2$  for the single-shell case,  $R_3$  for the two-shell case, etc.).

As a first test, we apply this optimization approach to the simple core–shell cloak (i.e., one core and one shell). It is not *a priori* clear that the described numerical optimization approach for arbitrary illumination via many different point-like illuminations yields the same result as Kerner's analytical result of the preceding section, which assumes homogeneous illumination. For  $R_2/R_1 = 1.5$ , we obtain an optimized diffusivity ratio of  $D_{2,\text{opt}}/D_0 \approx 2.8$ , compared to  $D_2/D_0 = 2.6$  before the optimization. The averaged standard deviation is reduced from  $\langle \Delta \rangle = 0.036$  to  $\langle \Delta_{\text{opt}} \rangle = 0.034$ . This closeness of the original and the optimized values indicates that there is not much to optimize with only one shell to start with. We also note that optimizing  $D_2/D_0$  for a core–shell cloak under inhomogeneous illumination will inevitably introduce deviations under homogeneous illumination.

At this point, it is also interesting to ask whether the performance of the single-shell cloak under arbitrary illumination conditions depends on the relative shell thickness. Some authors have stated (for the mathematically equivalent cases of stationary heat conduction [88] and magnetostatics [89]) that thinner shells yield better results. First, one should be aware that thinner shells require higher diffusivity contrasts according to Eq. (37), which tends to be more difficult to achieve experimentally at some point. Second, one must define which radius is fixed when changing the shell thickness. Figure 12 illustrates that the cloaking quality does indeed improve when reducing the outer radius  $R_2 \rightarrow R_1$  (and adjusting  $D_2$  following Eq. (37)) while fixing the inner radius  $R_1$ . In sharp contrast, when increasing the inner radius  $R_1 \rightarrow R_2$  (again adjusting  $D_2$ ) while fixing the outer radius  $R_2$ , the cloaking quality deteriorates. The latter case seems more meaningful to us because the overall size of the structure is fixed, whereas one compares structures with different overall sizes in the former case.

Next, we add a third layer, i.e., a second shell layer, with radius  $R_3$  and light diffusivity  $D_3$ . To again keep the overall size of the cloak fixed, we choose  $R_3/R_1 = 1.5$  (corresponding to  $R_2/R_1 = 1.5$  above). Hence, the intermediate radius  $R_2$  must obey the condition  $R_1 \leq R_2 \leq R_3$ . It is obvious that the choices  $R_2 = R_1$  or  $R_2 = R_3$  would again lead to a core plus a single shell only. Thus, we intuitively choose equally thick layers, i.e.,  $R_2 = (R_1 + R_3)/2$ .

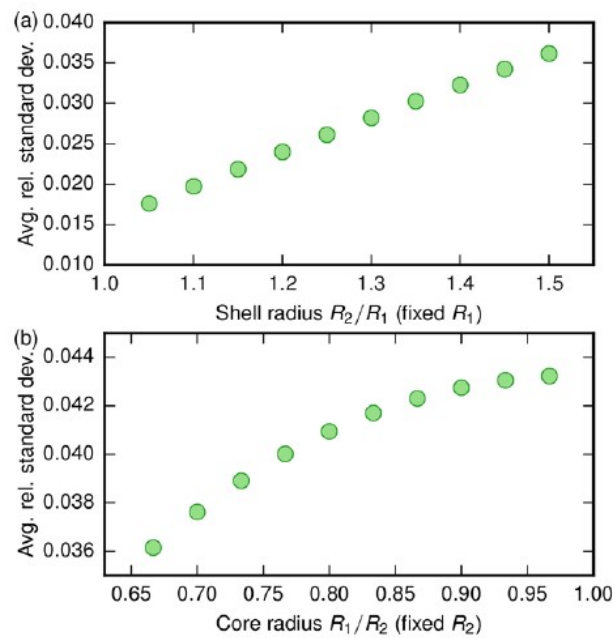


**Figure 12** Influence of the shell thickness on the cloaking performance of a core–shell cloak under inhomogeneous illumination. (a) For a fixed core radius  $R_1$ , thinner shells lead to better cloaking but also higher necessary diffusivity contrasts. (b) In contrast, for a fixed outer shell radius  $R_2$ , thinner shells lead to worse cloaking performance.

One could, however, also leave this parameter free in the optimization loop. We initialize both shell diffusivities with the original single-shell value obtained from diffusion theory, i.e.,  $D_2 = D_3 = 2.6 D_0$ .

Figure 13 shows the averaged relative deviation  $\Delta$  versus position of the light source for the obstacle, the single-shell cloak, the optimized single-shell cloak, and the optimized two-shell cloak. It can be seen that the relative deviations decrease only very slightly for the optimized single-shell cloak, while the two-shell cloak shows a significant improvement by a whole order of magnitude (from a maximum of 10% for the single-shell cloak to a maximum of 1.4% for the two-shell cloak). The remaining deviations ( $\langle \Delta_{\text{clk},2} \rangle = 0.0036$  as opposed to  $\langle \Delta_{\text{clk},1} \rangle = 0.034$ ) on the order of one percent are so small that we conclude that more than two shells may not be needed in practice. (Also, under homogeneous illumination, the two-shell cloak is not distinguishable from the reference.) In principle, however, the procedure could be continued to three-shell systems or beyond. One should be aware though that this step also implies going to thinner individual layers (keeping the ratio of outer radius to inner radius fixed), which means that the applicability of the light-diffusion approach may become questionable (see condition list in Sect. 2.1). It can already become questionable for single-shell structures optimized for large light throughput (i.e., for relatively low scattering particle concentrations and hence large transport mean free path lengths  $l_{\text{trans}}$ ). We will discuss this aspect using Monte Carlo simulations in Sect. 4.2, referring to the

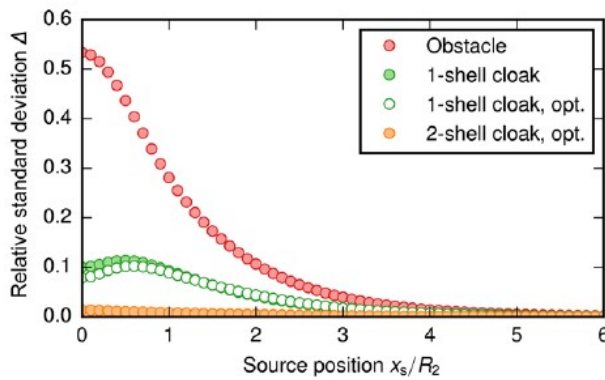


**Figure 13** Performance of multiple-shell cloaking structures. The average relative standard deviation with respect to the homogeneous reference is plotted versus the position of a point-like Gaussian illumination (see Fig. 11) for the obstacle structure (red data points), the original single-shell cloak (green data points,  $D_2 = 2.6 D_0$ ), a single-shell cloak with the shell diffusivity optimized for inhomogeneous illumination (light green data points,  $D_2 = 2.8 D_0$ ), and a two-shell cloak optimized for inhomogeneous illumination (orange data points,  $D_2 = 6.8 D_0$ ,  $D_3 = 0.46 D_0$ ). While optimizing the single-shell cloak does not yield significant improvements, the remaining deviations of the two-shell cloak are so small that adding yet more shells seems unnecessary. Parameters as in Fig. 11.

experiments shown in Sect. 3.1.2. Experimental results for a two-shell structure in the analogous case of stationary heat conduction are depicted in Fig. 14.

A slight variation of this optimization approach is to demand that the two-shell cloak must be perfect mathematically under conditions of homogeneous illumination. According to Refs. [65, 92] (and again assuming  $D_1 = 0$ ), this demand is fulfilled if the involved parameters are connected by

$$D_2 = D_3 \frac{R_2^2 + R_1^2 (D_0 + D_3)R_2^2 + (D_0 - D_3)R_3^2}{R_2^2 - R_1^2 (D_0 + D_3)R_2^2 - (D_0 - D_3)R_3^2}. \quad (40)$$

This condition effectively constrains the free variables. The remaining ones can then be used to optimize numerically the cloaking performance under inhomogeneous illumination conditions. For example, if we again choose  $R_2 = (R_1 + R_3)/2$  while fixing  $R_3/R_1$  and  $D_0$ , only a single free variable is left, namely  $D_3$ . The corresponding optimization results, however, are closely similar (not depicted) to those of the above more brute-force approach.

We note that yet another approach for designing few-shell cloaking structures for diffusion (of acoustic waves) has recently been discussed [93] (also see Ref. [94]). Their approach is based on the cancellation of multipole moments with increasing order, leading to analytical results for the connection between the shell radii and their diffusivities. For the closely related case of heat conduction, Ref. [72] discusses the design and realization of structures with as many as 10 concentric layers. Here, the result from the analytical transformation in Sect. 2.3 has been discretized

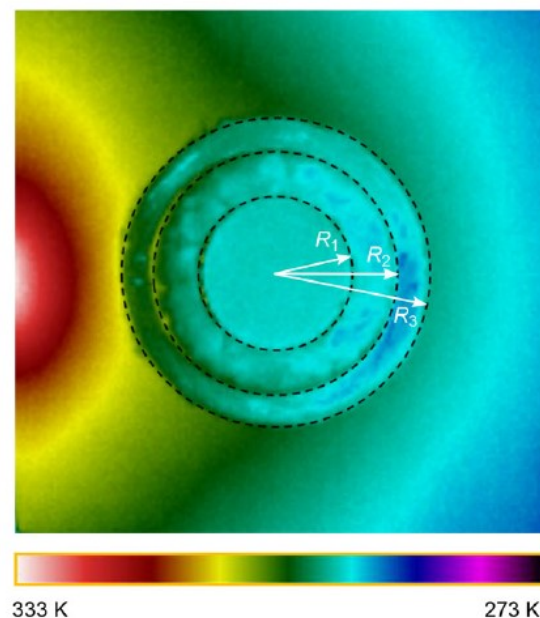


**Figure 14** Temperature distribution of a thermal cloak measured by a heat camera under conditions of a point-like heat source on the left. This leads to a large temperature gradient across the structure. The cloak is composed of one low-conductivity core and two shell layers with different thermal conductivity  $\kappa$  (see dashed circles). The corresponding radii are  $R_1 = 6$  mm,  $R_2 = 9.5$  mm, and  $R_3 = 12$  mm. In the stationary case, the heat conduction equation  $\bar{\nabla} \cdot (\kappa \bar{\nabla} T) = 0$ , for temperature  $T$ , is strictly analogous to Eq. (21) for light diffusion. Adapted with permission from Ref. [91]. Copyrighted by the American Physical Society.

into five pairs of layers. In each pair, the laminate formulas Eq. (24) and Eq. (25) have been applied.

Finally, mathematical work [95] suggests that the relative standard deviation between the behavior of a multi-shell cloak and that of the exact diffusivity-tensor distribution following from the spatial transformation scales inversely proportional to the number of layers in the limit of infinitely many layers. Recent detailed numerical calculations [96] for the case of stationary heat conduction (mathematically equivalent to stationary light diffusion) confirm this rather slow convergence for up to more than a thousand layers.

## 2.5. Invisible contacts on light-emitting diodes

In this example for the transformation-based design concept outlined in Sect. 2.3, we consider a potential application. Large-area organic light emitting diodes (OLEDs) are emerging as a novel type of light source for room lighting. One vision is to replace the white wallpaper in entire rooms by large-area OLEDs. However, due to the rather large electrical resistance of the conducting layers, one usually needs a grid of metallic contact lines on top. Obviously, these will cast a shadow and, instead of a homogeneous wall, one will look at some sort of metal grid, which may be undesired. The aim in this example [97] is to design a diffusive

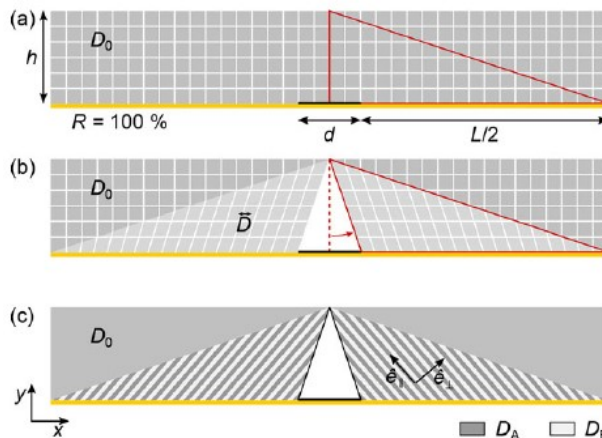


**Figure 15** Illustration of OLED contact cloaking. (a) Homogeneous diffusive layer (gray area) with diffusivity  $D_0$  on top of an OLED's light-emitting surface (yellow line, assumed reflectivity of 100% at the bottom) that is interrupted by metal contacts (black line). (b) Upon transforming the area indicated by the red triangle, a triangular hole is opened up that cloaks the metal contact. In the transformed area, the diffusivity becomes an anisotropic tensor. The white grid lines illustrate the transformation. (c) Realization of the diffusivity tensor with a piecewise-isotropic laminate structure with diffusivities  $D_A$  and  $D_B$ . The white triangle is isolated by a region with zero diffusivity (thin black line). Adapted from Ref. [97].

structure on top of the OLED and the contacts to homogenize the light emission such that one no longer sees the metal structures—neither in light emission nor in diffusive back-scattering from the OLED area when the lighting is switched off.

One might be tempted to think that to accomplish this goal, the core–shell cloaks discussed earlier could simply be cut in half and put on top of the OLED, with the core covering the contact wire. This approach does not work, however, since the diffusive current (proportional to the diffusivity) in such a cloak's shell is larger than in its surrounding (also see Fig. 11), whereas the incident photon current is constant everywhere outside the contact wire for the OLED surface. In other words, a cut through a core–shell cloak leads to three distinct regions with different diffusivities (core, shell, and surrounding), while the OLED surface features only two such regions, namely the wire and its surrounding.

Therefore, we start with a simple homogeneous diffusive layer (diffusivity  $D_0$ ) of height  $h$  on top of the OLED's light-emitting area (with an assumed reflectivity of 100%), which is interrupted by contacts of width  $d$  and spacing  $L$ . This untransformed structure is illustrated in Fig. 15(a) [97]. While such a layer “smears out” the shadow cast by the contact wire, only a very thick layer would lead to truly homogeneous emission. The red triangle indicates the part of the diffusive layer that is affected by the transformation illustrated in Fig. 15(b). This transformation maps the singular (and thus invisible) vertical center line onto a triangle with base length  $d$  and thus cloaks the light-blocking metal

contact:

$$x \rightarrow x' = \frac{2hLx + (h-y)(d^2 + dL)}{2h(L+d)}, \\ y \rightarrow y' = y. \quad (41)$$

Using Eq. (32), we immediately get the transformed diffusivity tensor  $\hat{\vec{D}}$ :

$$\hat{\vec{D}} = D_0 \begin{pmatrix} \frac{L}{L+d} + \frac{d^2(L+d)}{4h^2L} & -\frac{d(L+d)}{2hL} \\ -\frac{d(L+d)}{2hL} & \frac{L+d}{L} \end{pmatrix}. \quad (42)$$

We note that  $\hat{\vec{D}}$  depends only on the structural parameters  $L$ ,  $d$ , and  $h$  and is thus homogeneous (albeit anisotropic).

Diagonalization of Eq. (42) leads to the desired effective diffusivities  $D_{\parallel}$  and  $D_{\perp}$  parallel and perpendicular to the layers of an equivalent laminate structure. Using homogenization theory following Sect. 2.2, we can then calculate the laminate's constituent diffusivities  $D_A$  and  $D_B$ . The laminate's stacking direction is given by the diffusivity tensor's eigenvectors  $\hat{e}_{\parallel}$  and  $\hat{e}_{\perp}$ . For the (exaggerated) parameters used in Fig. 15 ( $d = 0.125 L$ ,  $h = 0.1875 L$ ), we obtain  $D_{\parallel} \approx 1.45 D_0$ ,  $D_{\perp} \approx 0.69 D_0$ , and an angle of  $40.8^\circ$  between the  $y$ -axis and  $\hat{e}_{\parallel}$ . For the laminate constituents, we then get  $D_A \approx 2.50 D_0$  and  $D_B \approx 0.40 D_0$ . Figure 15(c) illustrates the resulting structure with layer thickness  $L_A = L_B$  chosen. We note that the white triangle needs to have a diffusivity of zero (indicated by the thin black line) to prevent photons from entering this cloaked region.

Figure 16 displays results of numerical calculations performed with COMSOL Multiphysics, assuming a constant incident photon flux from the bottom of the structure and zero from the contact, and a top boundary with a photon-escape velocity of  $K = 3.63 \times 10^9$  cm/s. We plot the normalized photon density at the top boundary ( $y = h$ ), a value which is proportional to the perceived intensity of the OLED surface. Figure 16(a) shows the result for the untransformed case (blue curve), where the metal contact blocks the light flux and creates significant brightness variations. In contrast, the transformation leads to a perfectly homogeneous brightness (orange curve). In Fig. 16(b), results for laminate structures with two different layer thicknesses are shown as approximations of the continuous transformation. It becomes clear that for a proper homogenization, the layer thicknesses need to be decreased so much that the actual feasibility of such a structure might become questionable in terms of fabrication as well as of compatibility with a description by the diffusion equation (also see Sect. 2.1).

A related design based on piecewise-homogeneous anisotropic regions has recently been discussed in the context of transient thermal carpet cloaking [98].

Alternatively, it is also possible to obtain a perfectly homogeneous intensity distribution by replacing the

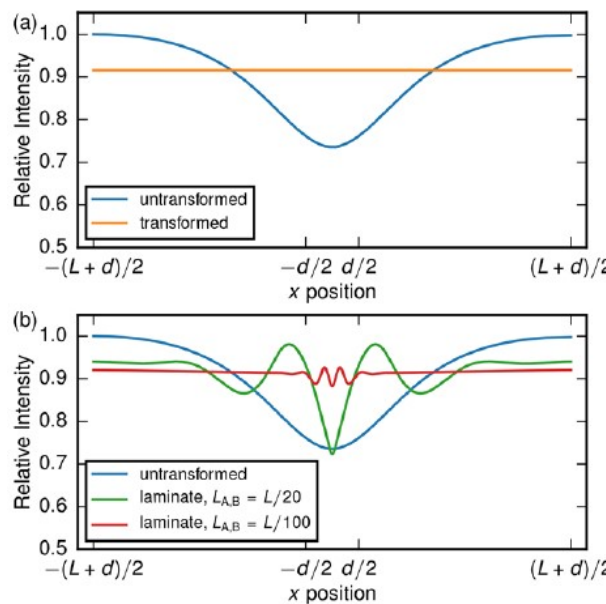


**Figure 16** Numerically calculated photon density at the top surface ( $y = h$ ) of the diffusive layer on top of the OLED active area. (a) The untransformed structure shows pronounced variations in intensity (blue curve) due to the shadowing of the metal contacts. In contrast, the transformed diffusivity tensor according to Eq. (42) results in a perfectly homogeneous brightness. The integral under both curves is the same. (b) Corresponding results for two laminate structures with different layer thicknesses  $L_A = L_B$  approximating the ideal transformation. Parameters are  $L = 0.5$  cm,  $d = 0.125L$ ,  $h = 0.1875L$ ,  $K = 3.63 \times 10^9$  cm/s,  $D_0 = 7 \times 10^7$  cm<sup>2</sup>/s,  $D_A = 2.5D_0$ , and  $D_B = 0.4D_0$ . Adapted from Ref. [97].

anisotropic tensorial diffusivity  $\vec{D}$  by a constant isotropic scalar diffusivity  $D_1$  according to [97]

$$\frac{D_1}{D_0} = \frac{(d + L)(d^2 + dL + 4h^2)}{4Lh^2}. \quad (43)$$

This approach is in close analogy to the core–shell cloaking as presented above.

Finally, we emphasize that many other devices can be designed using coordinate transformations. Examples are concentrators [99] and rotators [100]. In Fig. 17, we illustrate experimental results for a rotator in the equivalent case of heat conduction.

### 3. Experiments on core–shell cloaking

#### 3.1. Stationary conditions

We refer to conditions as stationary or quasi-stationary if the time scale of temporal changes is larger than the relevant effective characteristic time constant of the problem. One characteristic time constant is the diffusion time constant  $\tau_{\text{diff}}$  discussed in Sect. 2.1. A second characteristic time

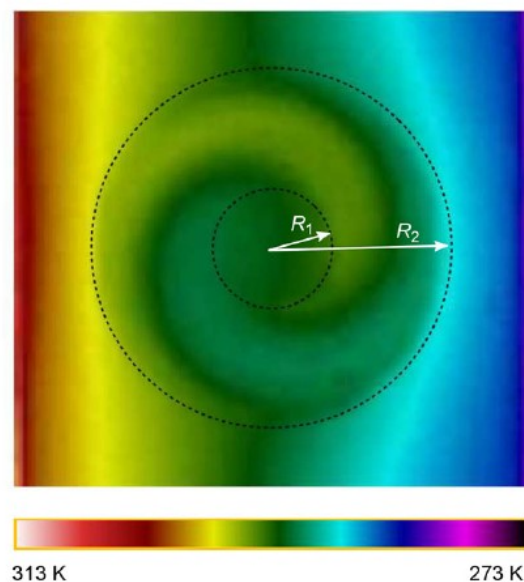


**Figure 17** Measured temperature distribution of a rotator composed of a thermal laminate metamaterial that is wrapped like a spiral (also compare Fig. 14). As a result, the heat flow near the center is opposite to the outside temperature gradient. The radii (see dashed circles) are  $R_1 = 0.8$  cm and  $R_2 = 2.7$  cm. Coordinate transformations enable the design of such rotators [100] as well as many other unusual devices. Adapted with permission from Ref. [101]. Copyrighted by the American Physical Society.

constant is the photon lifetime  $\tau$  (see Sect. 2.1). An effective characteristic time constant  $\tau_{\text{eff}}$  can be estimated by adding up the two corresponding rates, leading to

$$\tau_{\text{eff}} = \left( \frac{1}{\tau_{\text{diff}}} + \frac{1}{\tau} \right)^{-1}. \quad (44)$$

Even for macroscopic diffusive systems with centimeter dimensions,  $\tau_{\text{eff}}$  is typically around  $1 \times 10^{-9}$  s (see Sect. 3.2), such that even processes that cannot be resolved with the fastest presently commercially available high-speed optical cameras qualify as “stationary” for the purpose of light diffusion. This means that we can apply all the stationary results we have discussed in Sects. 2.2–2.4.2 to pretty much all ordinary-life conditions. Deviations from the stationary limit can be provoked though in dedicated experiments, which we shall describe in Sect. 3.2.

#### 3.1.1. Experiments in liquid diffusive media

To experimentally realize diffusive media, one needs to randomly distribute scattering particles in some dielectric background medium, for both of which one has a variety of choices. The spirit of the early experiments [58] to be reviewed in this section has been to choose a setting in which the diffusion approximation is well justified and in which the system parameters could be changed easily and quickly. We therefore used de-ionized water mixed with ordinary

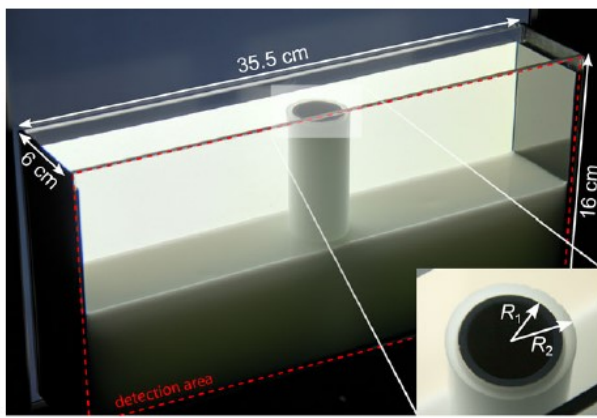


**Figure 18** Setup for water-based diffusive cloaking. A water-paint mixture inside an acrylic glass tank (only half-filled here for illustration) forms the surrounding, into which a painted aluminum core coated with microparticle-doped PDMS is embedded. Parameters are  $2R_1 = 32.1$  mm and  $2R_2 = 39.8$  mm. The dashed red rectangle indicates the detection plane of the camera. Reproduced from Ref. [58].

white wall paint (containing titania nanoparticles) for the diffusive background medium. The mixture was contained in a black acrylic glass tank with two transparent windows and was stirred continuously to avoid sedimentation of the particles. This also allowed us to easily vary the particle density and thus the diffusivity by adding more paint or diluting the solution.

For the cylindrical core, we used a hollow aluminum cylinder coated with white acrylic spray paint to make it diffusively reflecting. It later turned out that minimizing absorption on the core's surface is crucial for good cloaking performance (see Sect. 3.1.2).

Since two liquid diffusive media would intermix immediately, we used PDMS doped with melamine-resin microparticles for the cloaking shell. We thus obtained a solid core–shell structure embedded in a liquid surrounding. To homogeneously illuminate the whole system, we placed the water tank in front of a computer monitor allowing for various illumination conditions and took photographs of the light transmitted through the tank. To avoid edge effects originating from absorption of photons at the black lateral tank walls, we cropped all photographs by 25% from all sides. Figure 18 shows the experimental setup with a half-filled water tank and the core–shell cloak inside.

Figure 19(a)–(c) shows such photographs of the tank in the three configurations “reference” (empty tank), “obstacle” (the painted aluminum core in the tank), and “cloak” (the core–shell structure in the tank). In this setting with air as surrounding, both obstacle and cloak cast an obvious ballistic shadow. Due to its larger overall dimensions, the cloak’s shadow is even larger than that of the obstacle, illustrating the fact that any cloak can only work in the specific surrounding it has been designed for. We then filled the tank with water and gradually added white paint to increase the scatterer concentration until we found good cloaking. Figure 19(d)–(f) shows the results for a paint concentration

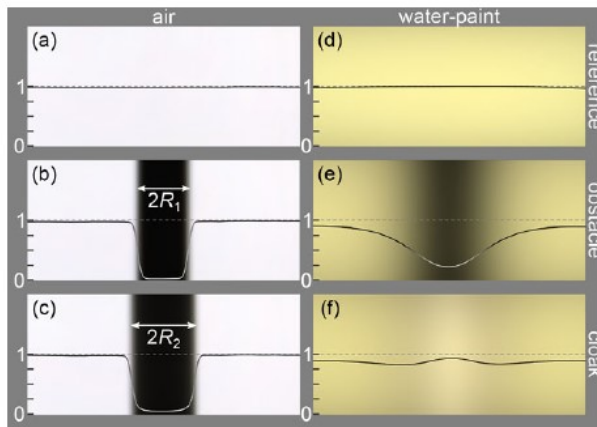


**Figure 19** Photographs of the water tank illuminated homogeneously with white light. In (a)–(c), the surrounding in the tank is air, while in (d)–(f), the tank is filled with a mixture of water and 0.35vol.% white wall paint, creating a scattering diffusive medium. The solid curves are intensity cuts along the dashed lines. For air in the tank, both obstacle (the painted aluminum cylinder) and cloak (a cylinder with an additional diffusive shell) are clearly detectable via their ballistic shadows. In contrast, for the diffusive water–paint surrounding, this shadow disappears for the cloak, which appears identical to the homogeneous reference except for variations of  $\pm 10\%$ . Reproduced from Ref. [58].

of 0.35vol.%. For this concentration, ballistic transmission measurements as described in Sect. 2.1 yielded a scattering mean free path of  $l_{\text{scat}} \approx 250 \mu\text{m} \ll L = 6 \text{ cm}$ , indicating that at least the surrounding was well in the diffusive limit. The reference still shows perfectly homogeneous transmission with a yellowish tint due to the wavelength-dependent scattering and absorption cross sections of the particles. Likewise, the obstacle’s shadow is still pronounced albeit “smeared out” due to diffusive instead of ballistic light transport in the tank. In contrast, the cloak does not cast a shadow any more but restores the homogeneous transmission of the reference except for small remaining color and intensity variations, proving that the core–shell approach to invisibility cloaking indeed works for light diffusion.

In Fig. 20, we show identical photographs as in Fig. 19, but for an inhomogeneous illumination pattern. Precisely, we illuminated the tank with a centered vertical bar with a width of about  $R_1$ . Consequently, the light is blocked completely by the obstacle and the cloak when there is only air in the tank (panels (a)–(c) of Fig. 20). With the diffusive water–paint surrounding, the line-like illumination is broadened to a bell-shaped transmission pattern for the reference, which is almost completely blocked by the obstacle but quite well reproduced by the cloak.

Figures 21 and 22 show results of numerical solutions of the diffusion equation, corresponding to the experiments under homogeneous and inhomogeneous illumination, respectively. For these calculations, the flexibility of our early experiments turned out to be a disadvantage. Due to the acrylic glass tank walls, we could not calculate the photon-escape velocity  $K$ , which in turn prevented us from fully

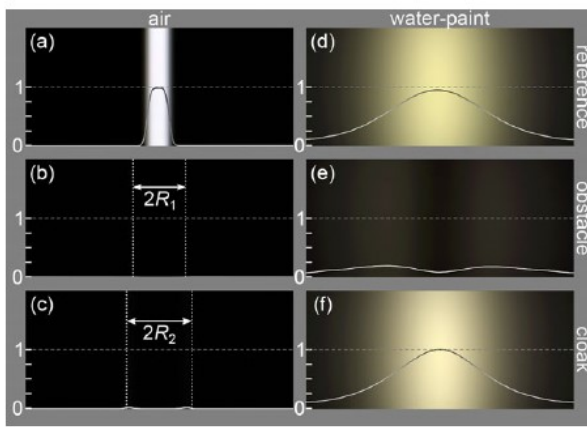


**Figure 20** Photographs as in Fig. 19, but for an inhomogeneous, line-like illumination pattern visible in panel (a). The obstacle blocks nearly all light in the ballistic as well as in the diffusive case, while the cloak reproduces the reference case fairly well for the diffusive water-paint surrounding. Reproduced from Ref. [58].

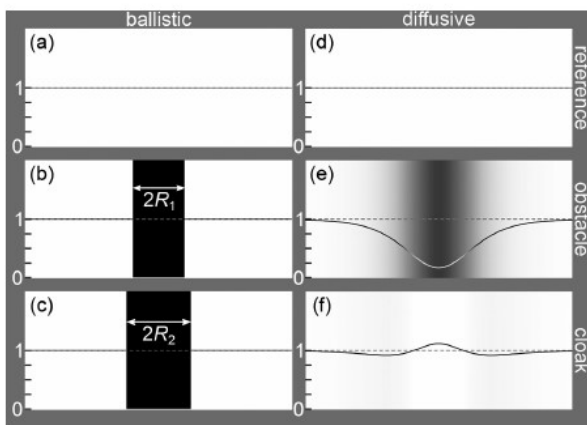


**Figure 21** Calculated photon densities  $n_{\text{phot}}(x, y, z = L)$  corresponding to the experimental results shown in Fig. 19. Panels (a)–(c) are just schemes following geometric optics. Parameters are  $L = 6 \text{ cm}$ ,  $2R_1 = 32.1 \text{ mm}$ ,  $2R_2 = 39.8 \text{ mm}$ ,  $D_0 = 5.27 \times 10^8 \text{ cm}^2/\text{s}$ ,  $D_2 = 72.1 \times 10^8 \text{ cm}^2/\text{s}$ ,  $\tau_0 = 10 \text{ ns}$ ,  $\tau_{12} = 0.245 \mu\text{s}$ , and  $K = 0.1 c_0$ .

characterizing the background medium according to Sect. 2.1.2. We found a diffusivity of  $D_0 = 5.27 \times 10^8 \text{ cm}^2/\text{s}$  but could not unambiguously obtain a value for the photon lifetime  $\tau_0$ . Furthermore, the shell diffusivity and the amount of absorption in the shell and on the core surface were unknown as well. Therefore, the parameters given in Figs. 21 and 22 have been obtained by comparison with the experimental results, both for the stationary case presented above and for the transient case to be presented in Sect. 3.2. Still, the numerical calculations fit well with the experimental results for both types of illumination.

It has to be noted, though, that the resulting diffusivity ratio of shell and surrounding of  $D_2/D_0 \approx 13.7$  is about three times larger than the value predicted by Eq. (37). Furthermore, we needed to introduce significant absorption at the core surface (via the photon lifetime  $\tau_{12}$ ) to match

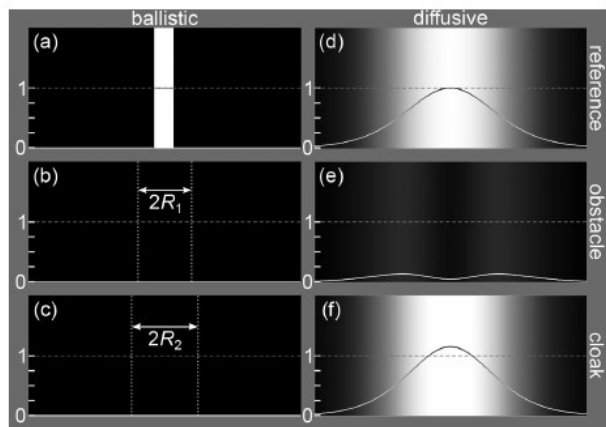


**Figure 22** Numerical results as in Fig. 21 (with identical parameters), but for inhomogeneous, line-like illumination. The results match the experimental outcome shown in Fig. 20 well.

the numerical to the experimental results. Intuitively, this absorption was compensated for by the higher diffusivity ratio  $D_2/D_0$ . The calculations showed that, in combination, these two aspects led to the remaining intensity variations visible for the cloak. Obviously, there is room for improvement by virtue of reducing the core absorption.

We note in passing that we also performed experiments on spherical instead of cylindrical samples. Since all effects were qualitatively identical but generally less pronounced there, we do not discuss the corresponding results here but rather refer to the original publication [58].

### 3.1.2. All-solid-state realizations

The early experiments described in the preceding section verified the core–shell cloaking principle but had various shortcomings as well. The water tank allowed for flexible parameter variations but it hindered full characterization of the contained medium and furthermore was not suited for any application, for which one really wants all-solid-state realizations. The overall diffusive transmittance was only around 0.5% due to the large tank dimensions and the high concentration of scattering particles in the water. The effects of absorption were quite pronounced, and the cloaking performance fell behind what seemed possible theoretically. All of these aspects have been improved by using the following approach [102], in which essentially all components were exchanged.

Figure 23 shows a photograph of the improved samples. First of all, we reduced the dimensions of the structures by a factor of about two in all directions to  $L_x = 15 \text{ cm}$ ,  $L_y = 8 \text{ cm}$ , and  $L_z = 3 \text{ cm}$ , yielding much more compact and easier to handle samples. We also exchanged the not-so-well-defined water–paint mixture by particle-doped PDMS and used the same particles in both shell and surrounding. Instead of particles inside white wall paint, we chose powdery titania nanoparticles (R700 from DuPont) with a mean diameter of 245 nm and low absorption [45].

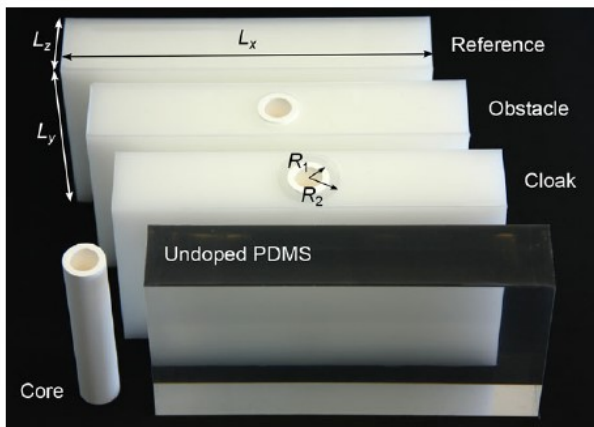


**Figure 23** Photograph of the fabricated all-solid-state samples for diffusive light cloaking next to a cuboid of undoped PDMS and an oxide-ceramic core for comparison. Parameters are  $L_x = 15$  cm,  $L_y = 8$  cm,  $L_z = 3$  cm,  $R_1 = 0.5$  cm, and  $R_2 = 1.2$  cm. Reproduced from Ref. [102].

This led to solid and thus stable samples on the one hand, but also to much easier characterization of the diffuse media due to the absence of the tank walls.

Earlier, we identified absorption at the core surface (and the thereby increased diffusivity ratio  $D_2/D_0$ ) as the main reason for the intensity variations that still distinguished the cloak from the reference. We therefore replaced the painted-aluminum core with one made from an oxide ceramic (Accuflect B6 from Accuratus Corporation, USA) with a specified diffuse reflectivity of more than 96% throughout the entire visible part of the electromagnetic spectrum. We could not find another suitable material with higher reflectivity specifications. To further reduce the necessary diffusivity contrast, we also chose a larger shell with  $R_2/R_1 = 1.5$  (formerly 1.25 [58]), leading to a predicted necessary diffusivity contrast of  $D_2/D_0 = 2.6$  (formerly 4.56 [58]). In the diffusive regime, this ratio directly translates to an identical contrast in the particle concentration, assuming that absorption is negligible. To maximize the diffuse transmittance, we chose the shell particle concentration as low as possible without compromising the cloaking performance. For a mass fraction of 0.1 mg/ml, we found the best cloaking performance for a ratio in particle mass fraction of  $C_0/C_2 = 3.9 = 1.5 \times 2.6$ . We will see in Sect. 4 that this deviation from theory mainly stems from the fact that with its low scatterer concentration, the shell cannot be described entirely by diffusion any more.

Figure 24 shows photographs of the samples under homogeneous white-light illumination. While the obstacle still shows a pronounced diffuse shadow, cloak and reference are indistinguishable with the naked eye, with no intensity or color variations visible. Furthermore, the smaller sample dimensions and reduced absorption lead to a much larger transmittance than for the water-based experiments, such that the samples can easily be inspected in daylight conditions. Figure 25 shows horizontal intensity cuts for the three samples. To quantify the transmittance, we compared

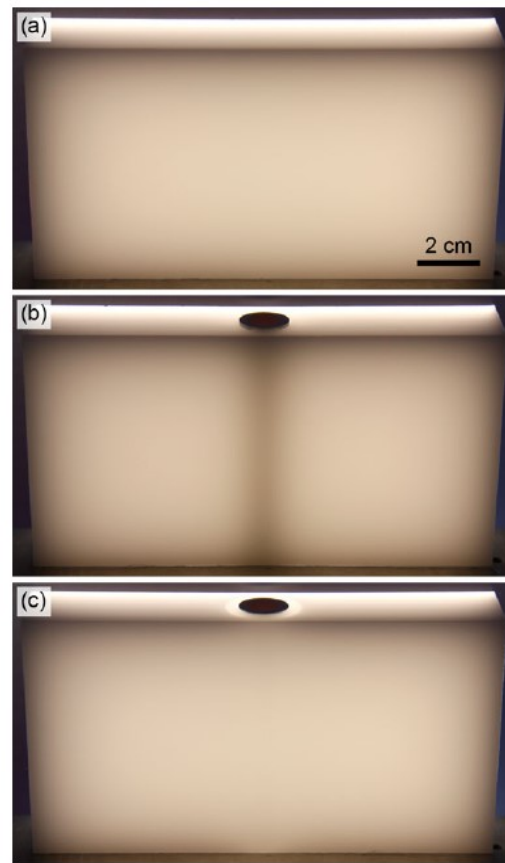


**Figure 24** Photographs of all-solid-state PDMS-based samples with high-reflectivity oxide-ceramic cores under homogeneous illumination. (a) Homogeneous reference sample with a particle mass fraction of  $C_0 = 0.39$  mg/ml. (b) Obstacle with a near-zero-diffusivity, high-reflectivity core casting a diffuse shadow. (c) With an additional shell with  $C_2 = 0.1$  mg/ml, the core's shadow vanishes. The sample shown in (c) is a nearly perfect macroscopic invisibility cloak for diffuse light. Reproduced from Ref. [102].

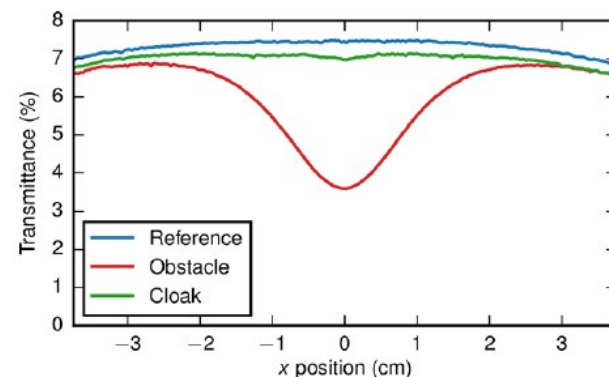


**Figure 25** Horizontal intensity cuts through the photographs shown in Fig. 24 (25% cropped from both sides), normalized to the light transmitted through an undoped PDMS cuboid. Compared to early water-based cloaking experiments, the transmittance increased by more than one order of magnitude. Reproduced from Ref. [102].

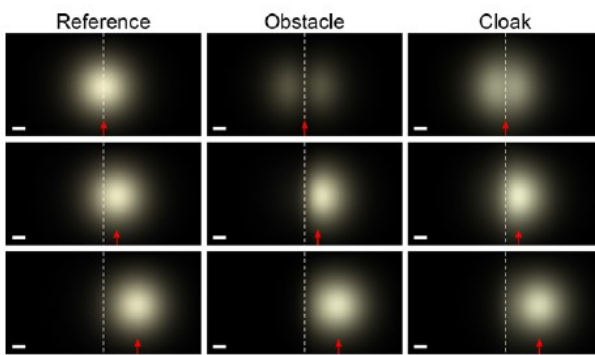


**Figure 26** Uncropped photographs of the PDMS-based samples under inhomogeneous, point-like illumination at different horizontal positions. The white dashed lines indicate the sample center, the red arrows mark the position  $x_s$  of the illumination spot. Cloaking works well with the strongest deviations from the reference for  $x_s = 0$ . For off-center illumination, the behavior of both obstacle and cloak converges to that of the reference. Length of the white scale bar: 1 cm.

the sample brightness to that of a transparent, undoped PDMS cuboid as shown in Fig. 23. We found a transmittance of about 7%, which is more than one magnitude larger than what we had in our early model experiments.

Using the approach of an average relative standard deviation defined in Eq. (39), we found  $\Delta_{\text{obs}} = 24.2\%$  for the obstacle and  $\Delta_{\text{clk}} = 4.35\%$  for the cloak. The rather large remaining deviation for the cloak mainly stems from the global offset between reference and both obstacle and cloak visible in Fig. 25. This offset results from inaccuracies in the fabrication of the diffusive surrounding for each sample, where the amount of liquid PDMS could not be determined with the desired precision.

We also measured how the PDMS-based samples perform under inhomogeneous illumination. Therefore, we focused a white-light source onto the sample and took photographs for different positions. Figure 26 shows example photographs of reference, obstacle, and cloak for three different source positions. As expected from Sect. 2.4.2, deviations of obstacle and cloak from the reference are strongest for source positions close to the sample center. Still, the cloak reasonably well reproduces the reference intensity pattern at any source position. For source positions further away from the sample center, all three samples look very similar since the influence of core and shell diminishes.

Finally, we point out that macroscopic (i.e., much larger than the operation wavelength) and broadband (i.e., working for all visible light) invisibility cloaks as presented above are not realizable for ballistic optics in air or vacuum [103]. There, superluminal wave velocities are necessary to compensate for the geometrical detour around the cloaked object, which is possible only for very small frequency intervals using resonant metamaterials. The strong dispersion of such metamaterials in turn leads to finite losses via the Kramers–Kronig relations, which would swallow almost all incident light for truly macroscopic cloaks. In contrast, the multiple scattering events in diffusive media effectively

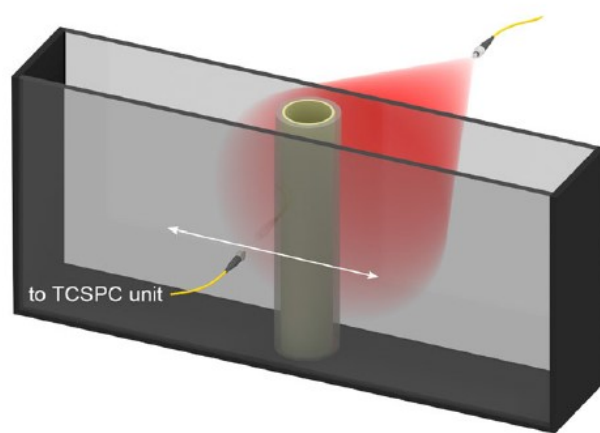


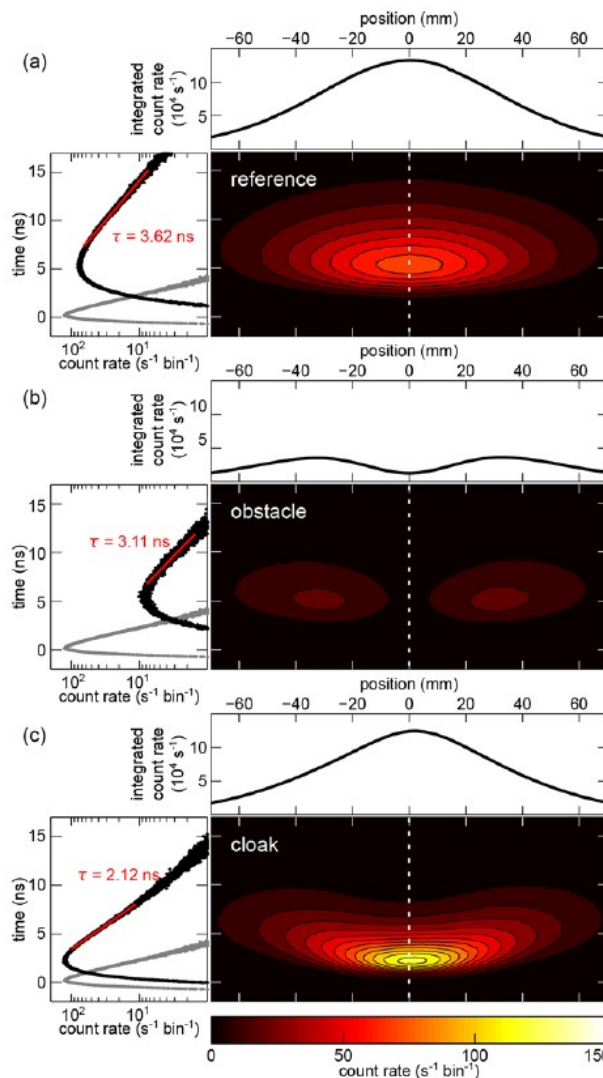
**Figure 27** Illustration of the measurement setup for transient diffusive-light cloaking. The water tank (or another diffusive medium) is illuminated with laser pulses emerging divergently from a fiber. The transmitted light is collected with a multimode fiber and fed into a time-correlated single-photon counting (TCSPC) unit. Horizontal scanning of the detection fiber yields spatial resolution. Reproduced from Ref. [104].

slow down light, which eliminates the need for superluminal velocities and thus for lossy resonant structures.

### 3.2. Transient conditions

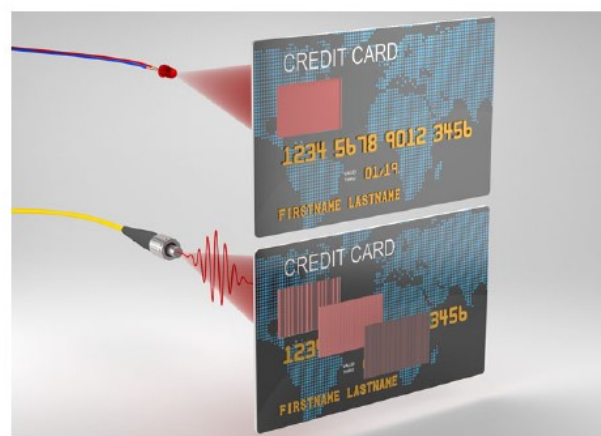
Does diffusive invisibility cloaking as demonstrated in the quasi-stationary experiments of Sects. 3.1.1 and 3.1.2 also work for transient conditions, i.e., for times shorter than the effective characteristic time constant  $\tau_{\text{eff}}$  (see Sect. 3.1)? We have already argued in Sect. 2.3 that the time-dependent light-diffusion equation is not form invariant under general spatial transformations, which indicates that transient diffusive-light cloaking should indeed not work. However, we have seen that cloaking under spatially inhomogeneous illumination works fairly well even though it is not compatible with the derivation of the core–shell cloak design. To experimentally investigate whether also transient cloaking might work rather well despite the mathematical considerations of Sect. 2.3, excitation as well as detection need to happen on time scales considerably smaller than  $\tau_{\text{eff}}$ . Here, we review experiments on the water-based cloaks which have been published in Ref. [104]. The all-solid-state structures generally show the same behavior, which is why we omit them in this section.

Figure 27 illustrates the experimental setup we used for measuring the transient response of the water-based structures. We illuminated the tank with pulsed laser light (640 nm wavelength, 50–500 ps pulse duration with a repetition rate of 10 MHz) emerging from a single-mode fiber, leading to a Gaussian spot with a full width at half maximum of 3.2 cm on the tank surface. We collected the transmitted light with a multimode fiber connected to a time-correlated single-photon counting (TCSPC) unit. Horizontally scanning the detection fiber yielded spatial resolution.



**Figure 28** Results of transient diffuse-light cloaking experiments. In each panel, the time-integrated data is displayed on the top, illustrating again that stationary cloaking works well also for inhomogeneous illumination. The temporally and spatially resolved photon count rate is displayed in color-coded contour plots, with  $t = 0$  being the time when the laser pulse maximum reaches the tank. Clearly, the cloak does not resemble the reference. It transmits incident light too quickly, leading to a higher and earlier maximum photon count rate and a lack of photons for later times. On the left-hand side of each panel, a cut along the dashed line in the contour plot is shown (black data points) together with the signal for an empty tank for comparison (gray data points). The decay time scales again illustrate the cloak's failure. Reproduced from Ref. [104].

The measurement results are displayed in Fig. 28. For each sample (panels (a)–(c)), the time-integrated signal corresponding to stationary illumination is shown on the top. Good agreement with the results from stationary inhomogeneous illumination (Fig. 20) prove again that stationary cloaking is working. The spatially and temporally resolved



**Figure 29** Artistic illustration of the potential application of diffusive core–shell cloaks as high-end security features. An arrangement (e.g., as a bar code) of miniaturized core–shell cloaks is invisible under normal, quasi-stationary illumination. Only under pulsed excitation and with time-resolved detection, cloaking fails and the arrangement is revealed.

data are displayed as false-color contour plots, with  $t = 0$  being the time when the laser pulse maximum reaches the tank. Unsurprisingly, the obstacle again transmits hardly any light and is clearly different from the reference. This time, however, also the cloak's results differ significantly from those of the reference. Specifically, the maximum photon count rate is larger and detected at earlier times than for the reference. In turn, the temporal decay afterwards is faster, leading to less transmitted light for later times. This difference is also clearly visible in the vertical cuts through the contour plots shown on the left-hand side of each panel. Intuitively, the high-diffusivity cloaking shell transmits incoming light too quickly, leading to an overshooting of the intensity and a lack of photons thereafter.

As stated earlier, the time-dependent light-diffusion equation is not form invariant under spatial transformations, and the experiments show that transient invisibility cloaking for diffuse light is not possible. Further numerical calculations [104] showed that this also applies to lossless structures and more sophisticated cloaks following the tools of transformation physics.

Besides the implications for diffuse optical tomography highlighted in Sect. 2.3, the transient failure of core–shell cloaks could actually be used for the creation of high-end security features. As shown in Fig. 29, miniaturized versions of our all-solid-state core–shell cloaks could be used to encode data, e.g., in the form of a bar code. This bar code would be invisible under everyday lighting conditions, but would reveal itself if illuminated with pulsed light and looked at with a time-resolved detection mechanism.

#### 4. Monte Carlo simulations

Looking at the list of criteria for diffusive light transport in Sect. 2.1, it becomes clear that the diffusion

approximation becomes shaky at some point when one successively reduces the concentration of scattering particles. Such a reduction may be desirable though to increase the diffuse light transmission (see Sect. 2.2) for applications. It is thus interesting to see how deviations from the diffusion description influence the performance of the invisibility devices discussed above. To investigate such deviations, one needs a more advanced level of description. Complete numerical solutions of the Maxwell equations for realistic distributions of scattering particles would be highly interesting, but getting them is far out of reach. In fact, even storing the refractive-index distribution of samples that are 4–5 orders of magnitude larger than the wavelength of light in all three dimensions and that contain a huge number of sub-wavelength scattering particles is a formidable task. The charm of Monte Carlo (MC) approaches lies in the fact that no such storage is needed.

#### 4.1. The Monte Carlo method for light transport

From the optical absorption and scattering properties of turbid media presented in Sect. 2.1, statistical probability distributions for the photon propagation can be derived [32]. Precisely, these distributions are

$$f_\theta = 2\pi p(\theta) \sin(\theta), \quad f_\varphi = \frac{1}{2\pi} \quad (45)$$

for the scattering angles  $\theta$  and  $\varphi$  ( $p(\theta)$  is the scattering phase function for isotropic particles) and

$$f_l = \mu_{\text{scat}} \exp(-\mu_{\text{scat}} l) \quad (46)$$

(with the scattering coefficient  $\mu_{\text{scat}} = 1/l_{\text{scat}}$ ) for the propagation step length  $l$  between two scattering events. These distributions provide the basis of an intriguingly simple scheme for the simulation of individual photon paths through scattering media.

- (1) Choose the photon's starting position  $\vec{r}$  and normalized direction  $\hat{v}$  according to the light source.
- (2) Randomly choose a step length  $l$  which statistically satisfies the probability function  $f_l$ .
- (3) Propagate the photon to  $\vec{r}' = \vec{r} + l\hat{v}$ .
- (4) Randomly choose a new direction  $\hat{v}$  via scattering angles  $\theta$  and  $\varphi$  satisfying the probability distributions  $f_\theta$  and  $f_\varphi$ .
- (5) Repeat steps 2–4 until the photon exits the medium, is absorbed, or exceeds a maximum propagation time.

By spatially binning the exit positions of the photons, transmission images corresponding to sample photographs as shown, for example, in Fig. 24 can be obtained. Absorption can be taken into account via the total traveled path length and the Lambert–Beer law given in Eq. (3).

It should be noted that, since light diffusion is a purely statistical process where all photons perform independent random walks, inspecting single-photon paths cannot yield any information about diffusive processes in a scattering

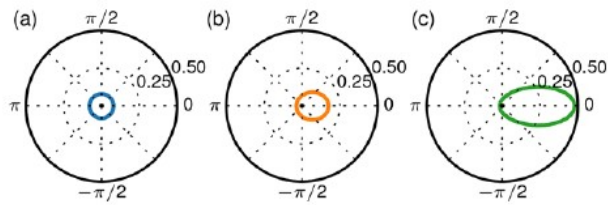


**Figure 30** Polar plots of the Henyey–Greenstein phase function for different scattering asymmetries: (a)  $g = \langle \cos \theta \rangle = 0$ , (b)  $g = 0.25$ , (c)  $g = 0.5$ .

medium. In other words, only by tracing a large number of photons and thereby faithfully reproducing the above probability distributions everywhere in the medium, can meaningful results for the photon-density distribution be obtained. For the same reason, inverse ray tracing, i.e., starting photons from the camera instead of from the light sources to decrease computation times, as is commonly done in ray-tracing software, is not possible in the case of disordered media.

The Monte Carlo method for photon transport is commonly used today in biomedical optics [105] and some implementations are freely available [106–108]. To specifically fit our needs in terms of diffusive light cloaking, however, we implemented a ray tracer ourselves in C++ which utilizes massive parallelization on graphics processors via the Nvidia CUDA platform. This platform also offers good and fast random-number generators. Since usually only uniformly distributed random numbers are available, these need to be mapped onto the desired distributions (Eqs. (45) and (46)) via inverse transform sampling [109]. Therefore, the above probability distributions need to be integrated and then inverted [32]. These steps are straightforward for the step length and the scattering angle  $\varphi$ , leading to

$$l(u) = -\ln(1-u)\mu_{\text{scat}} \quad (47)$$

and

$$\varphi(u) = 2\pi u. \quad (48)$$

Here,  $u$  is a uniformly distributed random number in the interval  $[0, 1]$ . To obtain the corresponding mapping for the scattering angle  $\theta$ , an expression for the scattering phase function  $p(\theta)$  needs to be found that is integrable and afterwards invertible. The Henyey–Greenstein phase function [110] provides such a function and also accommodates for asymmetric scattering via the asymmetry factor  $g = \langle \cos \theta \rangle$  (see Sect. 2.1). It was devised in 1941 to describe light scattering in interstellar dust clouds and is given by

$$p(\theta) = \frac{1}{4\pi} \frac{1-g^2}{(1+g^2-2g \cos \theta)^{3/2}}. \quad (49)$$

Figure 30 shows examples of the Henyey–Greenstein phase function for different values of the asymmetry factor  $g$ . From Eq. (49), the following rule for calculating

the cosine of the scattering angle  $\cos \theta$  from a uniformly distributed random number  $u$  is obtained:

$$(\cos \theta)(u) = \begin{cases} \frac{1}{2g} \left( 1 + g^2 - \left( \frac{1-g^2}{1-g+2gu} \right)^2 \right) & \text{if } g \neq 0, \\ 1 - 2u & \text{if } g = 0. \end{cases} \quad (50)$$

Besides the actual photon propagation according to the above ruleset, we implemented a simple library of constructive solid geometry [111] (CSG) primitives which can be combined via Boolean operations. With these, the reference, obstacle, and cloak geometry can easily be constructed without the need of a mesh-based or voxel-based discretization of space. Consequently, ray-intersection tests with the CSG tree have to be performed for every step in the photon tracing to determine whether a photon hits a medium boundary or not. Refraction and Fresnel-type reflection at such boundaries are taken into account via the refractive indices of the involved media. To model the high-reflectivity ceramic core, we furthermore allow completely opaque media with a Lambertian reflectivity of  $R \in [0, 1]$ . The slightly more realistic option of treating the core microscopically with a very high scattering coefficient (very small scattering mean free path) would increase the number of simulated scattering events and thus the calculation times drastically.

## 4.2. Comparison with experiment and diffusion theory

For the MC simulations, the optical properties of turbid media are sufficiently characterized by four parameters only: the scattering coefficient  $\mu_{\text{scat}} = 1/l_{\text{scat}}$ , the absorption coefficient  $\mu_{\text{abs}} = 1/l_{\text{abs}}$ , the asymmetry factor  $g = \langle \cos \theta \rangle$ , and the refractive index  $n$ . For the case of nanoparticle-doped PDMS, all of these parameters were experimentally accessible. We obtained the scattering coefficient via stationary ballistic transmission experiments (see Fig. 2), yielding  $\mu_{\text{scat},0} = 1.314 \text{ mm}^{-1}$  in the surrounding and  $\mu_{\text{scat},2} = 0.337 \text{ mm}^{-1}$  in the shell of our all-solid-state cloaks. By temporally and spatially resolved diffusive transmission measurements and comparison with theory (see Fig. 3), we obtained the absorption coefficient  $\mu_{\text{abs}} = 0.000445 \text{ mm}^{-1}$  and (via the diffusivity) the transport mean free path  $l_{\text{trans}} = 1.67 \text{ mm}$  in the surrounding. From the transport mean free path and the scattering mean free path, the asymmetry factor  $g = \langle \cos \theta \rangle = 0.544$  follows directly via Eq. (6). Finally, we assumed that the refractive-index change due to the added nanoparticles is negligible and thus used the textbook value for PDMS of  $n = 1.4$ . The only unknown parameter was the core reflectivity  $R$ , which we adjusted to match the MC output to the experimental results. We obtained the best match for a reflectivity of  $R = 98\%$ , which fits well to the manufacturer's specifications of the core material.

Figure 31 compares the MC simulation results for reference, obstacle, and cloak with corresponding transmittance photographs of the actual samples. For all three settings,

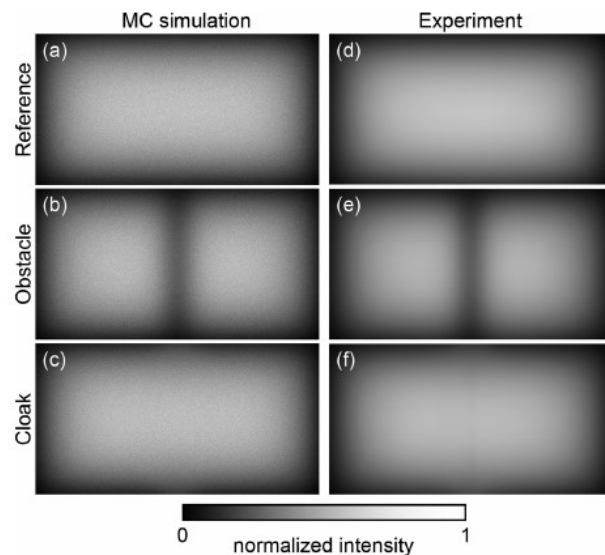


**Figure 31** Comparison of images obtained from Monte Carlo simulations with experimental results for the all-solid-state PDMS structures. (a)–(c) Transmission images obtained by tracing the paths of  $10^9$  photons emitted by a homogeneous Lambertian plane source behind the structures. Five out of these  $10^9$  photon random walks are illustrated in Fig. 32. Parameters are  $\mu_{\text{scat},0} = 1.314 \text{ mm}^{-1}$ ,  $\mu_{\text{scat},2} = 0.337 \text{ mm}^{-1}$ ,  $\mu_{\text{abs}} = 0.000445 \text{ mm}^{-1}$ ,  $g = 0.544$ ,  $n = 1.4$ , and  $R = 0.98$ . (d)–(f) Grayscale photographs of reference, obstacle, and cloak under homogeneous illumination.



**Figure 32** Selected simulated photon paths in three dimensions, projected onto the two-dimensional  $xz$ -plane for clarity. The path color qualitatively indicates time. Five photons enter the setup from the top. Out of these, two enter the cloak shell, two get transmitted, two get back-scattered out of the setup, and one exits at the right-hand side wall. The shell is shown in yellow, the hollow core in gray. Parameters as given in Fig. 31(c).

all relevant features are very well reproduced by MC simulations. For the cloak, five examples of simulated photon paths are depicted in Fig. 32. For a more detailed comparison of experiment and MC simulation, the left-hand side of Fig. 33 shows horizontal intensity cuts through the images in Fig. 31 (blue and orange curves for MC results and experimental results, respectively). To improve the signal-to-noise ratio for the MC results, we vertically integrated the MC images over a region well separated from the image borders to exclude any edge effects. We also horizontally cropped 25% from either side of the images. We normalized both sets of cuts individually to the cloak's maximum transmittance. Except for a global offset in the experimental reference curve (originating from fabrication inaccuracies, see Sect. 3.1.2), Monte Carlo theory and experiments fit extremely well.

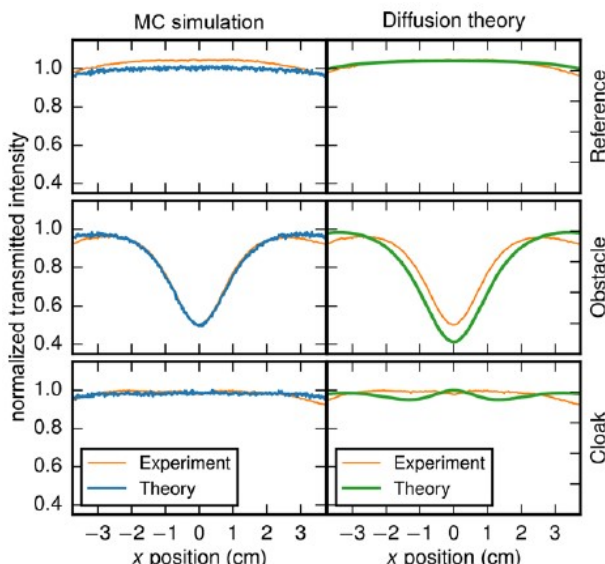


**Figure 33** Comparison of experimental results with MC simulations and diffusion theory. On the left-hand side, we compare intensity cuts through the MC images of Fig. 31 (blue curves) with experimental results as shown in Fig. 24 (orange curves). Except for a constant intensity offset for the reference, theory and experiment agree excellently. On the right-hand side, the same experimental curves are compared with numerical solutions of the diffusion equation (green curves) for  $D_0 = 1.19 \times 10^9 \text{ cm}^2/\text{s}$ ,  $D_2 = 3.9 D_0$ ,  $K = 3.63 \times 10^9 \text{ cm/s}$ ,  $\tau_0 = 10.5 \text{ ns}$ , and  $\tau_{12} = 0.23 \mu\text{s}$ . The differences for obstacle and cloak show that a purely diffusive model is not adequate for these experimental conditions.

On the right-hand side of Fig. 33, we additionally compare the experiments with corresponding numerical solutions of the diffusion equation. For these calculations, we used the experimentally determined photon lifetime  $\tau_0 = 10.5 \text{ ns}$  and surrounding diffusivity  $D_0 = 1.19 \times 10^9 \text{ cm}^2/\text{s}$  (see Fig. 3) and extrapolated the shell diffusivity via the ratio of particle mass fractions  $C_0/C_2 = 3.9 \equiv D_2/D_0$ . With a calculated photon loss velocity of  $K(n=1.4) = 3.63 \times 10^9 \text{ cm/s}$ , the core absorption—expressed as a photon lifetime  $\tau_{12}$  at the core surface—again was the only remaining parameter for the calculations. The intensity profiles presented in Fig. 33 (green curves) were obtained for  $\tau_{12} = 0.23 \mu\text{s}$ . Judging from the differences visible between experiment and diffusion theory for both obstacle and cloak, it is clear that a purely diffusive numerical model cannot adequately describe the actual samples any more. This is not particularly surprising since the shell's transport mean free path of  $l_{\text{trans}} = l_{\text{scat}}/(1-g) \approx 6.5 \text{ mm}$  is larger than the shell thickness of 4 mm and thus violates the requirements for diffusive transport outlined in Sect. 2.1, a situation which inherently cannot be covered by the diffusion equation. In contrast, Fig. 33 proves that this intermediate regime between diffusive and ballistic transport can very well be covered by Monte Carlo-based tracing of photons, which should consequently be the preferred numerical tool whenever a high overall light throughput and thus low scatterer concentrations are desired.

In light of its violation of the diffusion approximation and thus of its own design basis, it is surprising how well the all-solid-state cloak shown in Fig. 24(c) works after all. Intuitively, the lack of diffusive transport in the shell is compensated for by a yet lower shell particle concentration (1.5 times lower than what diffusion theory predicts) and thus yet less diffusive transport. Obviously, this compensation game cannot be played indefinitely and we suspect that the experiments shown above are already close to the configuration with maximum possible transmission yet reasonable cloaking performance.

## 5. Conclusions and outlook

Ordinary optical systems and devices operating in the regime of ballistic wave or ray optics are based on tailored spatial distributions of the refractive index  $n$  or the refractive-index tensor, e.g., designed by using (coordinate) transformations. In this review, we have shown that optical systems and devices in the regime of diffuse light scattering can be designed analogously by tailored spatial distributions of the light diffusivity  $D$  or the light-diffusivity tensor. Invisibility cloaking has served as a demanding benchmark example, which also has implications for the uniqueness of diffuse optical tomography.

It is interesting to compare ballistic and diffuse optics on a microscopic level. In both cases, we actually tailor the local density of dipoles to achieve some function. Zero dipole density leads to zero effect. In ballistic optics, the dipole density is proportional to  $(n-1)^2$ ; in diffuse optics it is inversely proportional to  $D$ . In ballistic optics, scattering is avoided by ordering the dipoles periodically (e.g., in crystals) or by dense packings of randomly arranged dipoles (e.g., in silica glass). In diffuse optics, we cultivate scattering—which is what this review is all about.

While the underlying principles of tailored diffuse optics have been discussed theoretically and thoroughly been tested experimentally, further experimental examples and especially further applications need to be worked out in the future. This might, for example, include light management in room-lighting systems. We have given a glimpse into this direction by the mentioned example of cloaked contacts on large-area light-emitting diodes. In essence, the contacts are made invisible by a clever redistribution of the flow of light made possible by intentionally spatially inhomogeneous distributions of scattering centers. To bring such ideas to real life, however, new fabrication techniques will need to be developed. The exploding field of 3D printing might give a boost. It is conceivable to print two different polymer materials, one with small and the other with large diffusivity for light, with a spatial resolution on the order of a few tens of micrometers. By digitally mixing the two materials, effectively any intermediate light diffusivity could be achieved; by lamination, even many anisotropic diffusivity tensors would become possible. Such approach would obviously be much more flexible than what has been reviewed here and it would also enable much more

complex architectures than the ones realized so far. Another application we have touched upon concerns high-end security items that contain information that is invisible to the human eye under ordinary illumination conditions. Again, 3D printing could be a key and enable individualized security items like hidden bar codes or hidden QR codes. The read-out process would also need to be made more practical, because the ultra-fast pulsed laser sources discussed in Sect. 3.2 are likely too expensive for practical implementations. It is conceivable that suitable illumination with coherent light also reveals the hidden information, but too little is currently known on the effects of coherence (like speckles and their correlations or open/dark channels) in such tailored structures with spatially inhomogeneous distributions of scattering centers.

Broadly speaking, mankind has been thinking about the design of optical systems and devices operating in the regime of ballistic light propagation for decades if not centuries. Thinking about the design of corresponding systems in the regime of diffuse light propagation has really just started recently. However, the concepts are on the table now.

**Acknowledgement.** We acknowledge support by the Deutsche Forschungsgemeinschaft (DFG) via the priority program DFG-SPP 1839 "Tailored Disorder", by the Hector Fellow Academy, and by the Karlsruhe School of Optics & Photonics (KSOP).

**Received:** 12 November 2015, **Revised:** 25 January 2016,  
**Accepted:** 15 March 2016

**Published online:** 22 April 2016

**Key words:** Light diffusion, Multiple scattering, Transformation optics, Invisibility cloaking, Tailored disorder.



**Robert Schittny** studied physics at the Karlsruhe Institute of Technology (KIT), obtaining his diploma in 2011. From 2012 to 2015 he worked in the group of Martin Wegener on mechanical metamaterials and invisibility cloaking beyond ballistic optics, where he received his PhD in physics in November 2015. He is an alumnus of the Karlsruhe School of Optics & Photonics (KSOP).



**Andreas Niemeyer** received his bachelor's degree in physics in 2012 from the Karlsruhe Institute of Technology (KIT). In 2015, he finished his master's degree at KIT with a thesis about the transient behavior of invisibility cloaks for diffusive light in the group of Martin Wegener. Since then, he has been studying tailored disorder in light-diffusive systems in the context of his PhD research.



**Frederik Mayer** was born in 1991 in Stuttgart, Germany. In 2010, he began studying physics at the Karlsruhe Institute of Technology (KIT) and obtained his bachelor's degree in 2014. Currently, he is working on his master's thesis in the field of diffusive-light cloaking in the group of Martin Wegener.



**Andreas Naber** earned his PhD in physics in 1994. From 1994 to 1999 he was a postdoctoral researcher at the Westfälische Wilhelms-Universität (WWU) Münster, Germany, and later on head of a research group with focus on nano-optics. In 2003 he was awarded the habilitation in physics. Since 2003 he has been a principal research scientist in the group of Martin Wegener at the Karlsruhe Institute of Technology (KIT). His research interests include nano-optical imaging techniques, single-molecule transport in biology, and light confinement in nanostructures.



**Muamer Kadic** graduated from the National Institute of Applied Science of Rennes. He worked as a research assistant at Trinity College Dublin, Ireland. In 2011, he received his PhD in optics and electromagnetism from Aix-Marseille University. He is currently working as a postdoctoral researcher in the group of Martin Wegener at Karlsruhe Institute of Technology (KIT). His research topics are mechanical metamaterials, plasmonics, and Hall-effect

metamaterials.



**Martin Wegener** completed his diploma and PhD in physics at Universität Frankfurt in 1986 and 1987, respectively. After being a postdoctoral researcher at AT&T Bell Laboratories in Holmdel, USA, he was a professor at Universität Dortmund from 1990 to 1995. Since 1995, he is a professor at Karlsruhe Institute of Technology (KIT). His research interests comprise solid-state physics, metamaterials, and optics.

## References

- [1] D. M. Schadt, B. Feng, and E. T. Yu, *Appl. Phys. Lett.* **86**(6), 063106 (2005).
- [2] H. A. Atwater and A. Polman, *Nat. Mater.* **9**(3), 205–213 (2010).
- [3] T. G. Deepak, G. S. Anjusree, S. Thomas, T. A. Arun, S. V. Nair, and A. S. Nair, *RSC Adv.* **4**(34), 17615–17638 (2014).

- [4] I. Schnitzer, E. Yablonovitch, C. Caneau, T. J. Gmitter, and A. Scherer, *Appl. Phys. Lett.* **63**(16), 2174–2176 (1993).
- [5] C. Huh, K. S. Lee, E. J. Kang, and S. J. Park, *Appl. Phys. Lett.* **93**(11), 9383–9385 (2003).
- [6] J. Zhou, N. Ai, L. Wang, H. Zheng, C. Luo, Z. Jiang, S. Yu, Y. Cao, and J. Wang, *Org. Electron.* **12**(4), 648–653 (2011).
- [7] J. H. Song, Y. C. Leem, Y. S. Park, H. M. Lee, W. Lim, S. T. Kim, G. Y. Jung, and S. J. Park, *J. Korean Phys. Soc.* **62**(5), 770–774 (2013).
- [8] S. J. Park, Y. D. Kim, H. W. Lee, H. J. Yang, J. Y. Cho, Y. K. Kim, and H. Lee, *Opt. Express* **22**(10), 12392–12397 (2014).
- [9] E. Hecht, *Optics* (Addison-Wesley, Essex, England 2002).
- [10] A. Nicolet, J. F. Remacle, B. Meys, A. Genon, and W. Legros, *J. Appl. Phys.* **75**(10), 6036 (1994).
- [11] A. Nicolet, F. Zolla, and S. Guenneau, *Eur. Phys. J. Appl. Phys.* **28**(2), 153–157 (2004).
- [12] J. B. Pendry, D. Schurig, and D. R. Smith, *Science* **312**(5781), 1780–1782 (2006).
- [13] U. Leonhardt, *Science* **312**(5781), 1777–1780 (2006).
- [14] V. M. Shalaev, *Science* **322**(5900), 384–386 (2008).
- [15] J. B. Pendry, A. Aubry, D. R. Smith, and S. A. Maier, *Science* **337**(6094), 549–552 (2012).
- [16] Y. Liu and X. Zhang, *Nanoscale* **4**(17), 5277–5292 (2012).
- [17] R. Fleury and A. Alù, *Prog. Electromagn. Res.* **147**, 171–202 (2014).
- [18] P. Kinsler and M. W. McCall, *Photon. Nanostruct.* **15**, 10–23 (2015).
- [19] D. Schurig, J. J. Mock, B. J. Justice, S. A. Cummer, J. B. Pendry, A. F. Starr, and D. R. Smith, *Science* **314**(5801), 977–980 (2006).
- [20] J. Li and J. B. Pendry, *Phys. Rev. Lett.* **101**(20), 203901 (2008).
- [21] J. Valentine, J. Li, T. Zentgraf, G. Bartal, and X. Zhang, *Nat. Mater.* **8**(7), 568–571 (2009).
- [22] L. H. Gabrielli, J. Cardenas, C. B. Poitras, and M. Lipson, *Nat. Photon.* **3**(8), 461–463 (2009).
- [23] T. Ergin, N. Stenger, P. Brenner, J. B. Pendry, and M. Wegener, *Science* **328**(5976), 337–339 (2010).
- [24] M. Wegener and S. Linden, *Phys. Today* **63**(10), 32–36 (2010).
- [25] T. Ergin, J. Fischer, and M. Wegener, *Phys. Rev. Lett.* **107**(17), 173901 (2011).
- [26] X. Chen, Y. Luo, J. Zhang, K. Jiang, J. B. Pendry, and S. Zhang, *Nat. Commun.* **2**, 176 (2011).
- [27] S. Mühlig, A. Cunningham, J. Dintinger, M. Farhat, S. B. Hasan, T. Scharf, T. Bürgi, F. Lederer, and C. Rockstuhl, *Sci. Rep.* **3**, 2382 (2013).
- [28] S. Chandrasekhar, *Radiative Transfer* (Oxford University Press, London/Dover, 1960).
- [29] A. Ishimaru, *Wave Propagation and Scattering in Random Media* (Academic Press, New York, 1978).
- [30] K. Furutsu, *J. Opt. Soc. Am.* **70**(4), 360–366 (1980).
- [31] R. F. Bonner, R. Nossal, S. Havlin, and G. H. Weiss, *J. Opt. Soc. Am. A* **4**(3), 423–432 (1987).
- [32] F. Martelli, S. D. Bianco, A. Ismaelli, and G. Zaccanti, *Light Propagation Through Biological Tissue and Other Diffusive Media: Theory, Solutions, and Software*, 1st edition (SPIE Press, Bellingham, WA, 2010).
- [33] J. R. Lorenzo, *Principles of Diffuse Light Propagation: Light Propagation in Tissues with Applications in Biology and Medicine* (World Scientific, Singapore 2012).
- [34] G. Mie, *Ann. Phys.* **330**(3), 377–445 (1908).
- [35] C. F. Bohren and D. R. Huffman (eds.), *Absorption and Scattering of Light by Small Particles* (Wiley-VCH, Weinheim, Germany, 1998).
- [36] M. Husnik, S. Linden, R. Diehl, J. Niegemann, K. Busch, and M. Wegener, *Phys. Rev. Lett.* **109**(23), 233902 (2012).
- [37] M. Husnik, J. Niegemann, K. Busch, and M. Wegener, *Opt. Lett.* **38**(22), 4597 (2013).
- [38] G. Zaccanti, E. Battistelli, P. Brusagli, and Q. Wei, *Pure Appl. Opt.* **3**(5), 897–905 (1994).
- [39] A. Fick, *Ann. Phys.* **170**(1), 59–86 (1855).
- [40] M. Bassani, F. Martelli, G. Zaccanti, and D. Contini, *Opt. Lett.* **22**(12), 853–855 (1997).
- [41] R. Graaff and J. J. T. Bosch, *Opt. Lett.* **25**(1), 43–45 (2000).
- [42] P. W. Anderson, *Phys. Rev.* **109**(5), 1492–1505 (1958).
- [43] D. S. Wiersma, P. Bartolini, A. Lagendijk, and R. Righini, *Nature* **390**(6661), 671–673 (1997).
- [44] M. Störzer, P. Gross, C. M. Aegerter, and G. Maret, *Phys. Rev. Lett.* **96**(6), 063904 (2006).
- [45] T. Sperling, W. Bührer, C. M. Aegerter, and G. Maret, *Nat. Photon.* **7**(1), 48–52 (2013).
- [46] R. Eichhorn, P. Reimann, and P. Hägg, *Physica A* **325**(1–2), 101–109 (2003).
- [47] A. Ros, R. Eichhorn, J. Regtmeier, T. T. Duong, P. Reimann, and D. Anselmetti, *Nature* **436**(7053), 928 (2005).
- [48] V. M. Shalaev, *Nat. Photon.* **1**(1), 41 (2007).
- [49] C. M. Soukoulis, S. Linden, and M. Wegener, *Science* **315**(5808), 47–49 (2007).
- [50] R. C. Haskell, L. O. Svaasand, T. T. Tsay, T. C. Feng, B. J. Tromberg, and M. S. McAdams, *J. Opt. Soc. Am. A* **11**(10), 2727–2741 (1994).
- [51] A. Kienle and M. S. Patterson, *J. Opt. Soc. Am. A* **14**(1), 246–254 (1997).
- [52] F. Martelli, A. Sassaroli, G. Zaccanti, and Y. Yamada, *Phys. Med. Biol.* **44**(5), 1257–1275 (1999).
- [53] D. Contini, F. Martelli, and G. Zaccanti, *Appl. Opt.* **36**(19), 4587–4599 (1997).
- [54] J. D. Jackson, *Classical Electrodynamics* (Wiley, New York, 1998).
- [55] A. Kienle, *J. Opt. Soc. Am. A* **22**(9), 1883–1888 (2005).
- [56] R. B. Bird, W. Stewart, and E. N. Lightfoot, *Transport Phenomena*, 1st edition (Wiley, New York, 2002).
- [57] B. Palsson and S. Bhatia, *Tissue Engineering* (Pearson Prentice Hall, Upper Saddle River, NJ, 2004).
- [58] R. Schittny, M. Kadic, T. Bückmann, and M. Wegener, *Science* **345**(6195), 427–429 (2014).
- [59] S. Harris, *An Introduction to the Theory of the Boltzmann Equation* (Courier Corporation, Mineola, New York, USA 2004).
- [60] J. W. Goodman, *J. Opt. Soc. Am. A* **66**(11), 1145–1150 (1976).
- [61] W. Choi, A. P. Mosk, Q. H. Park, and W. Choi, *Phys. Rev. B* **83**(13), 134207 (2011).
- [62] M. Kim, Y. Choi, C. Yoon, W. Choi, J. Kim, Q. H. Park, and W. Choi, *Nat. Photon.* **6**(9), 581–585 (2012).

- [63] Y. Choi, T. R. Hillman, W. Choi, N. Lue, R. R. Dasari, P. T. C. So, W. Choi, and Z. Yaqoob, *Phys. Rev. Lett.* **111**(24), 243901 (2013).
- [64] K. P. Vemuri and P. R. Bandaru, *Appl. Phys. Lett.* **104**(8), 083901 (2014).
- [65] G. W. Milton, *The Theory of Composites* (Cambridge University Press, Cambridge, 2002).
- [66] V. G. Veselago, *Sov. Phys. Usp.* **10**(4), 509–514 (1968).
- [67] R. T. Thompson and M. Fathi, *Phys. Rev. A* **92**(1), 013834 (2015).
- [68] S. Guenneau, C. Amra, and D. Veynante, *Opt. Express* **20**(7), 8207–8218 (2012).
- [69] H. Chen and C. T. Chan, *Appl. Phys. Lett.* **91**(18), 183518 (2007).
- [70] A. Greenleaf, Y. Kurylev, M. Lassas, and G. Uhlmann, *Commun. Math. Phys.* **275**(3), 749–789 (2007).
- [71] M. Kadic, T. Bückmann, R. Schittny, and M. Wegener, *Rep. Prog. Phys.* **76**(12), 126501 (2013).
- [72] R. Schittny, M. Kadic, S. Guenneau, and M. Wegener, *Phys. Rev. Lett.* **110**(19), 195901 (2013).
- [73] S. R. Arridge, *Inverse Problems* **15**(2), R41 (1999).
- [74] T. Durduran, R. Choe, W. B. Baker, and A. G. Yodh, *Rep. Prog. Phys.* **73**(7), 076701 (2010).
- [75] B. Pollak, *CHEST* **24**(6), 663 (1953).
- [76] J. P. Culver, R. Choe, M. J. Holboke, L. Zubkov, T. Durduran, A. Slemp, V. Ntziachristos, B. Chance, and A. G. Yodh, *Med. Phys.* **30**(2), 235 (2003).
- [77] R. Choe, S. D. Konecky, A. Corlu, K. Lee, T. Durduran, D. R. Busch, S. Pathak, B. J. Czerniecki, J. Tchou, D. L. Fraker, A. DeMichele, B. Chance, S. R. Arridge, M. Schweiger, J. P. Culver, M. D. Schnall, M. E. Putt, M. A. Rosen, and A. G. Yodh, *J. Biomed. Opt.* **14**(2), 024020 (2009).
- [78] M. Cope and D. T. Delpy, *Med. Biol. Eng. Comput.* **26**(3), 289–294 (1988).
- [79] J. C. Hebden, *Psychophysiology* **40**(4), 501–510 (2003).
- [80] A. Siegel, J. J. Marota, and D. Boas, *Opt. Express* **4**(8), 287 (1999).
- [81] J. B. Fishkin and E. Gratton, *J. Opt. Soc. Am. A* **10**(1), 127–140 (1993).
- [82] B. W. Pogue and M. S. Patterson, *Phys. Med. Biol.* **39**(7), 1157–1180 (1994).
- [83] V. Ntziachristos, X. Ma, and B. Chance, *Rev. Sci. Instrum.* **69**(12), 4221–4233 (1998).
- [84] F. E. W. Schmidt, M. E. Fry, E. M. C. Hillman, J. C. Hebden, and D. T. Delpy, *Rev. Sci. Instrum.* **71**(1), 256–265 (2000).
- [85] A. P. Calderón, *Comput. Appl. Math.* **25**(2–3), 133–138 (2006).
- [86] R. Schmied, J. C. Halimeh, and M. Wegener, *Opt. Express* **18**(23), 24361–24367 (2010).
- [87] E. H. Kerner, *Proc. Phys. Soc. B* **69**(8), 802–807 (1956).
- [88] H. Xu, X. Shi, F. Gao, H. Sun, and B. Zhang, *Phys. Rev. Lett.* **112**(5), 054301 (2014).
- [89] F. Gömöry, M. Solovyov, J. Souc, C. Navau, J. Prat-Camps, and A. Sanchez, *Science* **335**(6075), 1466–1468 (2012).
- [90] T. Bückmann, M. Kadic, R. Schittny, and M. Wegener, *Proc. Natl. Acad. Sci. USA* **112**(16), 4930 (2015).
- [91] T. Han, X. Bai, D. Gao, J. T. Thong, B. Li, and C. W. Qiu, *Phys. Rev. Lett.* **112**(5), 054302 (2014).
- [92] K. Schulgasser, *J. Phys. C: Solid State Phys.* **10**(3), 407 (1977).
- [93] L. Kroon, *Cancellation of acoustic waves in scattering media*, in: International Congress on Metamaterials, Oxford, UK, 2015.
- [94] X. Wang and P. Schiavone, *Z. angew. Math. Phys.* **64**(3), 895–903 (2013).
- [95] M. A. Pakhnin and T. A. Suslina, *St. Petersburg Math. J.* **24**, 949–976 (2013).
- [96] D. Petiteau, *Ingénierie de métamatériaux thermiques: transformations d'espace et techniques d'homogénéisation appliquées à l'équation de la chaleur*, Ph.D. thesis, Aix Marseille Université, Marseille, France (2015).
- [97] F. Mayer, R. Schittny, A. Egel, A. Niemeyer, J. Preinfalk, U. Lemmer, and M. Wegener; *Adv. Opt. Mater.*, DOI: 10.1002/adom.201500652 2016.
- [98] S. Guenneau, D. Petiteau, M. Zerrad, C. Amra, and T. Purirajasinghe, *AIP Adv.* **5**(5), 053404 (2015).
- [99] H. Chen, B. Hou, S. Chen, X. Ao, W. Wen, and C. T. Chan, *Phys. Rev. Lett.* **102**(18), 183903 (2009).
- [100] Y. Luo, J. Zhang, B. I. Wu, and H. Chen, *Phys. Rev. B* **78**(12), 125108 (2008).
- [101] S. Narayana and Y. Sato, *Phys. Rev. Lett.* **108**(21), 214303 (2012).
- [102] R. Schittny, A. Niemeyer, M. Kadic, T. Bückmann, A. Naber, and M. Wegener, *Opt. Lett.* **40**(18), 4202 (2015).
- [103] H. Hashemi, B. Zhang, J. D. Joannopoulos, and S. G. Johnson, *Phys. Rev. Lett.* **104**(25), 253903 (2010).
- [104] R. Schittny, A. Niemeyer, M. Kadic, T. Bückmann, A. Naber, and M. Wegener, *Optica* **2**(2), 84–87 (2015).
- [105] C. Zhu and Q. Liu, *J. Biomed. Opt.* **18**(5), 050902 (2013).
- [106] Q. Fang and D. A. Boas, *Opt. Express* **17**(22), 20178–20190 (2009).
- [107] Q. Fang, *Biomed. Opt. Express* **1**(1), 165–175 (2010).
- [108] A. Doronin and I. Meglinski, *Biomed. Opt. Express* **2**(9), 2461–2469 (2011).
- [109] L. Devroye, *Non-uniform Random Variate Generation* (Springer, New York, 1986).
- [110] L. C. Henyey and J. L. Greenstein, *Astrophys. J.* **93**, 70–83 (1941).
- [111] J. D. Foley (ed.), *Computer Graphics: Principles and Practice*, 2nd edition, Addison-Wesley Systems Programming Series (Addison-Wesley, Reading, MA, 1995).